Basin-scale hydrodynamics and physical connectivity in a Great Patagonian Lake

Javiera Abarca[a], Hugo N. Ulloa[b], Yarko Niño[a,c,d]

[a]*Department of Civil Engineering, Faculty of Physical and Mathematical Sciences, Universidad de Chile, Santiago 8370449, Chile*
[b]*Department of Earth & Environmental Science, University of Pennsylvania, Philadelphia, USA.*
[c]*Advanced Mining Technology Center, Universidad de Chile, Santiago, Chile*
[d]*Advanced Center for Water Technologies, Santiago 8370448, Chile*

Abstract

Patagonian lakes are one of the most unexplored aquatic environments on Earth, and little is known about their thermo-hydrodynamics and current trophic state. Meanwhile, increasing urbanization and industrialization in their catchments compromise their health. Here, we investigate Lake Llanquihue, one of the Earth's great freshwater bodies in Northern Patagonia, Chile. Still considered a pristine environment, Llanquihue has experienced recent contamination events along its littoral, whose impacts remain unknown. In response, public and private agencies have started to develop tailor-made monitoring plans to survey water quality. However, without comprehensive knowledge of the lake's functioning, it is impossible to determine the fate and effects of contaminants in the water body. Here, we characterize via numerical simulations the basin-scale hydrodynamics of Lake Llanquihue, crucial information for diagnosing the transport of dissolved and suspended matter within its basin. Aiming to delimit the regions impacted by contaminated discharges, we pose a fundamental question that applies to any lake: *What is the physical connectivity between two zones of interest within a lake?* To address this question, we introduce a framework that characterizes the preferential pathways and quantifies the timescale tracers take to stream from one zone to another within an aquatic system. This framework is applied to investigate the physical connectivity among the main urban and rural settlements connected to the littoral zone of Lake Llanquihue. Our results show that the physical connectivity between long-distance littoral regions is primarily controlled by a time-persistent, large-scale gyre and seasonal mesoscale gyres. The above information will enable lake managers to monitor the health of the water basin, identify and notify potential risk zones impacted by polluted effluents, and advance toward a more sustainable relationship with Lake Llanquihue.

Keywords: Northern Patagonian Lake, Annual thermohydrodynamics, Physical connectivity

1. Introduction

Patagonia is one of the most unexplored regions on Earth, and its aquatic systems are still considered pristine (Iriarte, 2018; García et al., 2019). Yet, the expanding urbanization and industrialization in Patagonian lakes' catchments compromise the stability of essential freshwater ecosystems. Today, the scarcity of integrated knowledge of Patagonian water bodies precludes a sound outlook on their physical and biogeochemical functioning and response to short-term and long-term anthropogenic stressors. This paper contributes to establishing the physical background for one of the

*Corresponding author: ulloa@sas.upenn.edu

most human-stressed lakes in Northern Patagonia and one of the Great lakes on Earth, Llanquihue (Herdendorf, 1982). Over the last few years, Lake Llanquihue has faced several contamination events in its littoral waters. However, these effluents' pathways and impacted areas still need to be delimited. The latter information is crucial to warn promptly stakeholders that interact and depend intimately upon the lake's water health and authorities to take proper protection measures. To address this issue, we must access the lake's hydrodynamics. We thereby posit a fundamental quest for any lake affected by effluents: *What is the physical connectivity between two zones of interest within a lake?* Here, we develop a general framework to investigate the physical connectivity between different zones within a lake basin and integrate it into simple metrics, such as preferential trajectories and timescales. Based on this framework, we investigate the physical connectivity between various littoral zones within Lake Llanquihue in direct contact with urban and rural settlements.

Figure 1: (a) Aerial photo of Lake Llanquihue and (b) aerial photo of the Puerto Varas waterfront, Chile. Contamination episode of unregulated greywater discharge in Lake Llanquihue, September 2019 (source:www.biobio.cl).

Lake Llanquihue, also known as '*The blue mirror of Patagonia*' (Figure 1a), is located in northern Patagonia (41°08'S 72°47'W, 51 m.a.s.l.), and it is the largest freshwater body of the so-called Lake District (Figure 2a) and the second largest lake in Chile (Campos, 1984). Guarded by the imposing snowcapped Osorno and Calbuco volcanoes to the east and surrounded by the green southern-central valley along its western shore (Figure 2a), Lake Llanquihue charms its inhabitants and visitors with a stunning landscape (Ballesteros, 2019). Its basin, carved during the last glaciation (Porter, 1981), has a surface area of 870.5 km^2, a volume of 159 km^3, a shoreline of about 197 km, a maximum fetch of 42 km, and maximum and mean depths of 317 m and 182 m, respectively (Campos et al., 1988). Hosted by a temperate oceanic climate, Lake Llanquihue is fed by significant annual rainfall and a network of small streams that descend from the Andes Mountains and inflow the lake's basin along the east shore–the Blanco River being the main contributor. In contrast, the lake has only one outflow–the Maullin River–located southwest of the basin, which leads the lake's waters to the Pacific Ocean (Almanza et al., 2019). The residence time of the lake's stored water is approximately 74 years (Soto and Campos, 1995). The above metrics make Lake Llanquihue a 'great lake' (Herdendorf, 1982) and one of the most important freshwater sources in the Austral Hemisphere.

Table 1: Summary of physical properties of Lake Llanquihue

Property	**Units**	**Range**	**Observation/Source**
Location	(Lat/Lon)	41°08'S-72°47'W	www.igm.cl
Altitude	(m.a.s.l.)	51	www.igm.cl
Volume	(km^3)	159	(Campos et al., 1988)
Surface	(km^2)	870.5	(Campos et al., 1988)
Shoreline	(km)	197	(Campos et al., 1988)
Maximum fetch	(km)	42	(Geller, 1992)
Equivalent radius	(km)	16.65	$R_e = \sqrt{A_{\mathrm{surf}}/\pi}$
Maximum depth	(m)	317	(Campos et al., 1988)
Mean depth	(m)	182	h_m, (Campos et al., 1988)
Lake steepness	(m)	5.5×10^{-3}	$\lambda = h_m/(2\,R_e)$
Thermocline depth (summer)	(m)	30-40	h_t, www.dga.cl/lagos
Transparency-Seiche depth	(m)	8-30	www.dga.cl/lagos
Temperature	(°C)	10-20	www.dga.cl/lagos
Conductivity	$(\mu\mathrm{S\,cm}^{-1})$	38-110	www.dga.cl/lagos
Mixing regime	(-)	Monomictic	(Geller, 1992)
Main inflow: Blanco river	$(\mathrm{m}^3\,\mathrm{s}^{-1})$	1.8	www.cenma.cl
Main outflow: Maullin river	$(\mathrm{m}^3\,\mathrm{s}^{-1})$	79-132	mma.gob.cl/maullin
Residence time	(year)	74	(Soto and Campos, 1995)
Inertial period	(h)	18.2	T_f for latitude: 41°08'S
Internal Rossby radius	(km)	2.22-5.03	$R_i = c_i/f$ (winter-summer)
Burger number	(-)	0.13-0.30	$\mathcal{B} = R_i/R_e$ (winter-summer)
Stratification aspect ratio	(-)	0.22	h_t/h_m, (summer)
Gravest internal Kelvin wave period	(h)	49-50	summer, Figures 6 and 7
Gravest internal Poincaré wave period	(h)	17.2-17.5	summer, Figures 6 and 7
Characteristic large-scale gyre radius	(km)	9.87-10.34	R_{LSC}, (winter-summer) upper layer
Characteristic mesoscale gyre radius	(km)	4.33-4.57	R_{MAC}, (summer-winter) upper layer
Outer orbital period of large-scale gyre	(h)	479 – 743	T_{LSC}, (winter-summer) upper layer
Outer orbital period of mesoscale gyre	(h)	212 – 240	T_{MAC}, (winter-summer) upper layer

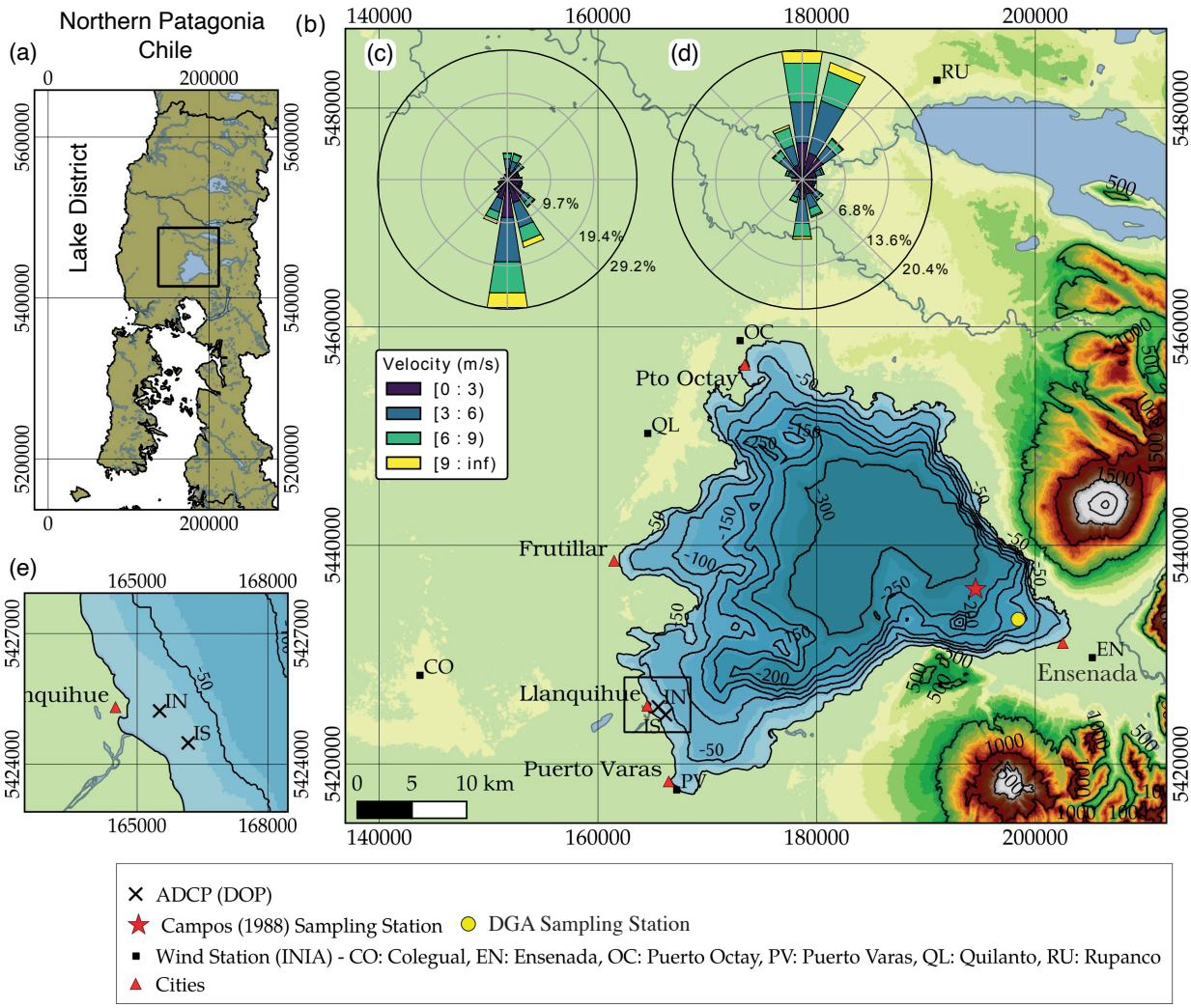

Figure 2: (a) Regional location of Lake Llanquihue. (b) Location and bathymetry of Lake Llanquihue along with meteorological station (CO: Colegual, QL: Quilanto, OC: Octay, RU: Rupanco, and EN: Ensenada) and ADCP (IN: Iansa Norte and IS: Iansa Sur) locations. Time-averaged 'wind rose' for winds in the center of the lake for the periods (c) May to August and (d) December to March. (e) Close-up of ADCP stations IN and IS.

The general physical features of Lake Llanquihue were described more than 30 years ago in the pioneering limnological work by Campos et al. (1988). Since then, the observations reported by Campos et al. (1988) remain the only available monthly characterization of the annual thermal cycle in Lake Llanquihue. Although new in situ observations exist, data are scattered in a few public reports, making them hard to connect. Llanquihue has a monomictic thermal mixing regime and still enjoys deep blue transparent waters (Figure 1a), with a mean Secchi depth of approximately 21 m and a range of 8-30 m (DGA-2018). During the winter, from late June to late September in the Southern Hemisphere, the cold Austral winds stir (explorador-climatico) and cool the lake surface, causing vertical mixing and bringing the upper water column to minimum temperatures of approximately 10°C. The spring season provides days with a high level of solar radiation, fostering the formation of weak thermal stratification between

October and November. The stratification becomes stronger throughout the summer, from late December to late March. In this period, the surface water temperature reaches up to 20°C in February, with a thermocline at approximately 40 m in depth. Once autumn falls, the lake stratification weakens. However, its signature lasts until the end of June, thus closing the annual thermodynamic cycle of Lake Llanquihue. Before the present study, the hydrodynamics and general circulation of the lake's waters were unknown. However, based on the lake thermodynamics, length scales, and latitude, we anticipate that Earth rotation must affect basin-scale motions.

Lake Llanquihue provides various services, including freshwater supply, greywater disposal from water treatment plants, transportation, pisciculture, fishing, and recreation (Donoso, 2018). However, providing these services has come at a cost; pristine and oligotrophic waters are being stressed by increasing human activities along the lake's shore. Studies indicate that Lake Llanquihue could progress towards a mesotrophic state (De los Ríos and Soto, 2007) due to the pervasive increase in nutrient loads and biomass production observed over the last decades (Woelfl et al., 2013). In addition to the degradation of the trophic state, the western littoral region has faced unprecedented discharges of untreated effluents that present potential threats to the population (Figure 1b). However, the lack of a standardized and high-frequency monitoring program (currently twice per year) and a centralized data portal hamper our ability to determine the fate and impact of these unforeseen discharges and track the long-term evolution of the trophic and physical state of Lake Llanquihue.

Understanding the basin-scale hydrodynamics of Lake Llanquihue is critical for developing an effective and tailor-made monitoring program. Addressing this challenge is especially relevant for determining the water pathway of the most anthropogenically stressed littoral areas. The western shore, hosting the major cities around the lake's littoral (Figure 2b), has been recently affected by untreated urban wastewater discharges (terram.cl). On the other hand, the northern and eastern sides of the basin host fishing farms, which are sources of nutrients and potential drivers of bottom degradation (www.biobio.cl). In both cases, there is no characterization of the nutrient-enriched waters and debris from human activities. Characterizing lake circulation (Beletsky et al., 1999; Laval et al., 2003) is, therefore, key for establishing monitoring points and examining the physical connectivity among sites of potential pollution sources, water uptake, food supply, leisure areas, and ecosystem niches.

The first goal of this article is to provide a first overview of the hydrodynamics of Lake Llanquihue. We achieve this goal by integrating the available data into an annually-based, three-dimensional, and high-resolution numerical model. The second and broader goal is to address the fundamental problem of untangling the physical connectivity between different regions in a lake to determine whether an effluent discharged in site 'A' reaches site 'B'. We address this problem by using a comprehensive numerical framework and introducing new physical metrics that can be applied to any aquatic system. Therefore, in addition to providing a practical tool for characterizing the physical functioning of Lake Llanquihue, our model grants a unique opportunity to examine the physical connectivity between strategic regions of the lake basin. Summing up, this study (i) establishes a physical baseline and a reference point for future studies of Lake Llanquihue; (ii) supports policymakers to elaborate tailored monitoring program (e.g., Norma Secundaria Lago Llanquihue) and achieve the sustainable development goals VI, XI, and XIV defined by the United Nations (sdgs.un.org); (ii) introduces a framework to investigate the physical connectivity among distinct zones within a lake's

basin; and last but not least (iii) expands the knowledge of Southern Hemisphere lakes.

The paper is organized as follows. In Section 2, we describe atmospheric forces, the modeling approach, and the input data to constrain the numerical solutions. In the same section, we introduce the concept of physical connectivity in aquatic systems. The numerical modeling results are reported in Sections 3 and 4. First, we focus on characterizing the basin-scale hydrodynamics (3.1) and the seasonality of the large-scale circulation (3.2). Secondly, we investigate the physical connectivity among various critical littoral zones in Lake Llanquihue via tracer experiments (4.1 and 4.2). Lastly, we discuss the implications of our results and outline the conclusions in Sections 5 and 6, respectively.

2. Data and Methods

This section briefly describes the meteorological forcing and the in situ observations used to calibrate the basin-scale numerical model. Appendix A provides links to access the meteorological forcing data and summarizes numerical model settings, including the variables and parameters used to compute the net surface heat flux, H_n. Additionally, Supplementary Material A reports wind patterns and the daily and annual net surface heat flux cycle for 2015/2016.

2.1. Meteorological forcing

Meteorological data of relative humidity, air temperature, solar radiation, and winds were obtained from public access weather stations located in the vicinity of Lake Llanquihue. These stations are Quilanto (QL), Colegual (CO), Ensenada (EN), Rupanco (RU), and Puerto Octay (OC). Their locations are shown in Figure 2. The cloud cover needed to compute the net heat exchange between the lake and the atmosphere was obtained from the local airport 'El Tepual'. All meteorological data have a 1 h time-averaged resolution.

On a seasonal scale, northerly winds are predominant during the austral summer, i.e., from late December to late March (Figure 2c), whereas southerly winds dominate from the autumn to winter seasons (Figure 2d). On a daily scale, wind systematically peaks during the daytime and ceases at night, resembling diurnal land-lake breezes. The signature of such a diurnal wind cycle shows up in a sharp energy peak at 24 h for both the Autumn/Winter and Spring/Summer periods (2015/2016) (S.3, Supplementary Material A).

Lake Llanquihue experienced a broad range of net surface heat flux, H_n, reaching values up to 900 $\mathrm{W\,m^{-2}}$ in January (summer) and minimum values of -500 $\mathrm{W\,m^{-2}}$ in April (autumn) (Supplementary Material A, Figure S.4). An evident heating period begins around late September and extends until February. During this period, H_n increases and fosters the progressive heating of surface waters and thermal stratification. From February onward, H_n starts to decline. The peak in heat loss occurs at night between March and April, i.e., from late summer to early autumn in the austral hemisphere. During the above period, the heat loss rate works at maximum thermal expansivity (Bouffard and Wüest, 2019; Doda et al., 2022). The latter leads to a peak in surface buoyancy flux and maximal available potential energy production (Winters et al., 1995) that drives thermally induced convective motions, vertical mixing (Biemond et al., 2021; Ulloa et al., 2022), and the consequent deepening of the surface mixed layer during autumn. Between late autumn and early winter, the lake transfers heat to the atmosphere at a lower rate, yet deep mixing and the thermal

homogenization of the water column continue until late winter (see Figure 3). The annually-integrated surface heat flux closes with a residual of approximately 1 W m^{-2}.

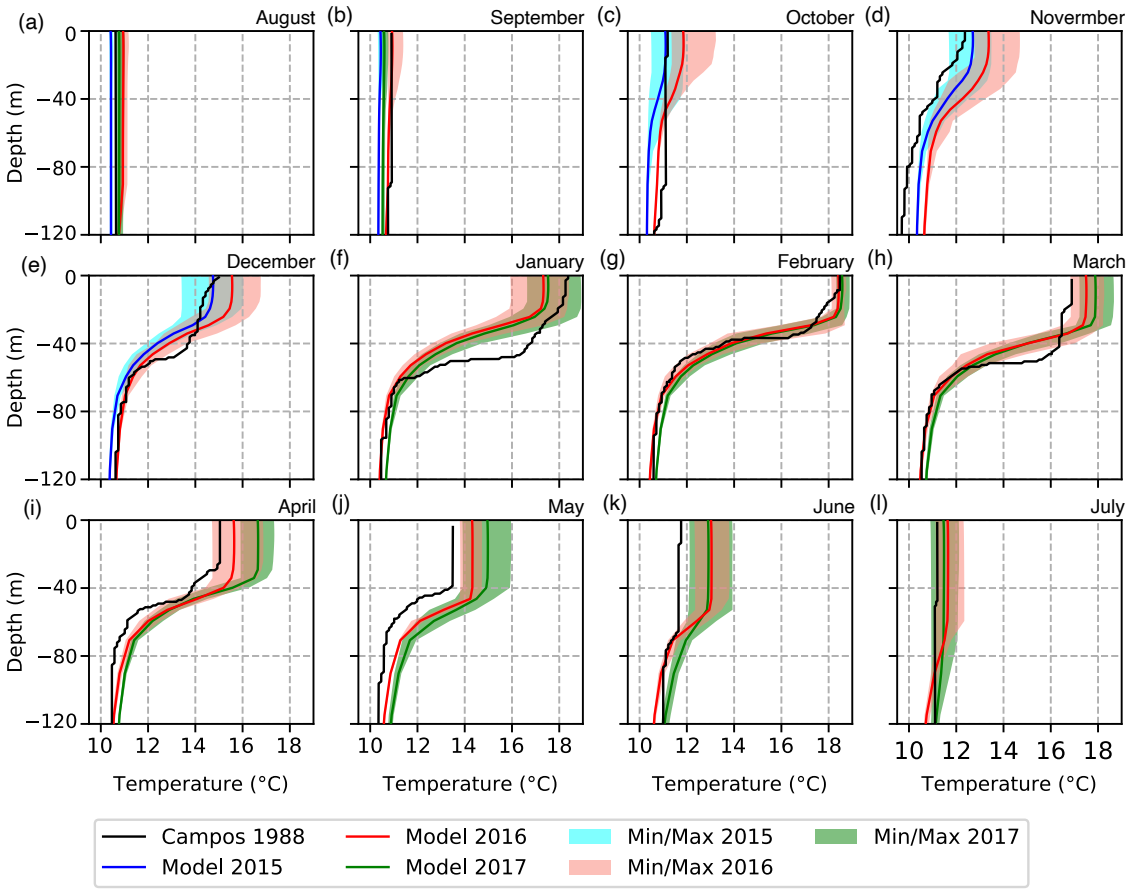

Figure 3: Monthly temperature profiles. Observations by Campos et al. (1988) in black, CTD casts by the local monitoring program in the dashed line, and model results in blue (2015), red (2016), and green (2017).

2.2. Lake in-situ observations

Our study integrates three available in-situ data sets. First, we profited from the monthly temperature profiles reported by Campos et al. (1988) to have annual-based lake temperature evolution, shown in Figure 3. Second, we used the biannual temperature profiles (August and March) measured by the Lake Llanquihue monitoring program in 2016 and 2017 (Supplementary Material A, Figure S.7). Third, we utilized two short-term ADCP records collected by the Division of Ports Works, Ministry of Public Works, Chile, during the Austral winter (August/27-September/26) and the Austral summer (February/7-March/8) of 2016. The ADCP was deployed in the nearshore of the southwest basin (Figure 2e) at a depth of approximately 8 m, and the data is reported in Appendix B. To our knowledge, these in-situ observations are the only public hydrodynamic data available from Lake Llanquihue.

2.3. Numerical modeling

Using realistic numerical simulations, we modeled and characterized the basin-scale and annual thermohydrodynamics of Lake Llanquihue. Considering the lake size, latitude, and steepness (Table 3), we used the comprehensive DELFT3D-FLOW numerical solver in its hydrostatic version to integrate the three-dimensional (3D) Reynolds-averaged Navier-Stokes (RANS) equations in an f-plane for an incompressible fluid within the Boussinesq limit (Deltares, 2014). The momentum and heat equations were discretized on an Arakawa-C grid of uniform horizontal grid resolution of $\Delta x = \Delta y = 130$ m. We employed a stretched z-coordinate grid for the vertical domain that enhanced the spatial resolution in those regions where the temperature and the flow presented the highest gradients. The minimum and maximum sizes of the vertical grids were $\min(\Delta z) = 3$ m and $\max(\Delta z) = 81$ m, respectively. We adopted Delaunay-type triangulation to interpolate the lake bathymetry on the mesh grid (e.g., Weatherill, 1992). Subgrid turbulence was modeled using a second-order k-ϵ, including buoyancy effects on the turbulence closure. The governing equations were integrated using an implicit finite difference scheme (ADI) on the staggered grid. Recent applications of DELFT3D to model lake hydrodynamics include Baracchini et al. (2020); Amadori et al. (2020); Rey et al. (2021).

Our lake model considered neither inflows nor outflows since we did not have information on inflows nor continuous measurements of the only lake outflow–the Maullin River. Nonetheless, considering that the modeling period (2 years) is substantially shorter than the lake's residence time (74 years), it is reasonable to ignore the residual flow field that small inflows and the outflow may induce in the water basin, except in the very mouth of the outflow. Therefore, we assumed a closed basin with a no-flux boundary condition at the lake bottom. As discussed later, bottom friction was modeled and calibrated using a Chézy roughness coefficient, C_r. The wind surface stress $\boldsymbol{\tau}_s$ was modeled as $|\boldsymbol{\tau}_s| = C_D\, \rho_a\, |\boldsymbol{U}_{10}|^2$, with C_D being the drag coefficient estimated using the bulk formulae in Large and Pond (1981), ρ_a being the air density, and $\boldsymbol{U}_{10}$ being the wind velocity field at 10 m above the surface. The model was forced by a spatially and time-varying wind field. The spatial distribution of wind was obtained from a linear interpolation of in situ meteorological data around the lake. In addition, since the wind speed in the center of a lake is higher than the speed at the shoreline (e.g., Shimizu et al., 2007), wind data from meteorological stations to the lake center were weighted by a factor obtained from the publicly accessible weather research forecasting 'Explorador Eólico' (eolico.minenergia.cl). This factor was obtained by correlating the wind forecast at the lake center with wind forecasts at nearby weather stations. The wind over the lake surface did not include the correction factor for wind magnitudes lower than 1.0 m s^{-1}. Likewise, we modeled the heat flux exchange at the lake surface, both spatial- and time-varying, using atmospheric forcing information from the surrounding meteorological stations.

We thus resolved the 3D unsteady basin-scale hydrodynamics comprising wind- and buoyancy-driven flows. The numerical model does not integrate small-scale processes like internal waves breaking. Yet, their impact on the vertical momentum balance and mixing is parameterized (refer to Deltares, 2014).

2.4. Model initialization and calibration

The model was initialized from rest with an entirely homogeneous water temperature $T_0 = 10.5$°C and a background salinity that was assumed to be negligible for the winter conditions reported by Campos et al. (1988). From these initial

conditions, the dynamical variables were integrated in time from August 2015 to August 2017 (modeling period) using a time step $\Delta t = 1$ min. This two-year period allowed us to first "warm-up" the model from winter 2015 to winter 2016 and compare the results with the available ADCP observations in Lake Llanquihue during February and August 2016. To calibrate the numerical model, we run nine cases to find the Chézy coefficient C_r that maximizes the model skill metric (MSM) (Willmott, 1981):

$$\mathrm{MSM} = 1 - \frac{\sum |v_{\mathrm{mod}} - v_{\mathrm{obs}}|^2}{\sum (|v_{\mathrm{mod}} - \bar{v}_{\mathrm{obs}}| + |v_{\mathrm{obs}} - \bar{v}_{\mathrm{obs}}|)^2}\,, \tag{1}$$

for the numerically resolved velocity field during the periods with ADCP measurements. v_{mod} and v_{obs} represent the modelled and observed velocity components, respectively. Whereas $\bar{v}_{\mathrm{mod}}$ and $\bar{v}_{\mathrm{obs}}$ are their corresponding time averages over the sampling periods. These periods correspond to the summer observations - from February 7 to March 8 - and the winter observations - from August 27 to September 26 - of 2016. In every case, the numerical experiments were forced using the meteorological data described in section 2.1. We achieved a maximum MSM of approximately 0.61 for $C_r \approx 150$, as shown in Figure A.1 (Appendix A). Thus, we run the second year (August 2016-July 2017) to extend the modeling period, adopting the above optimal Chézy coefficient.

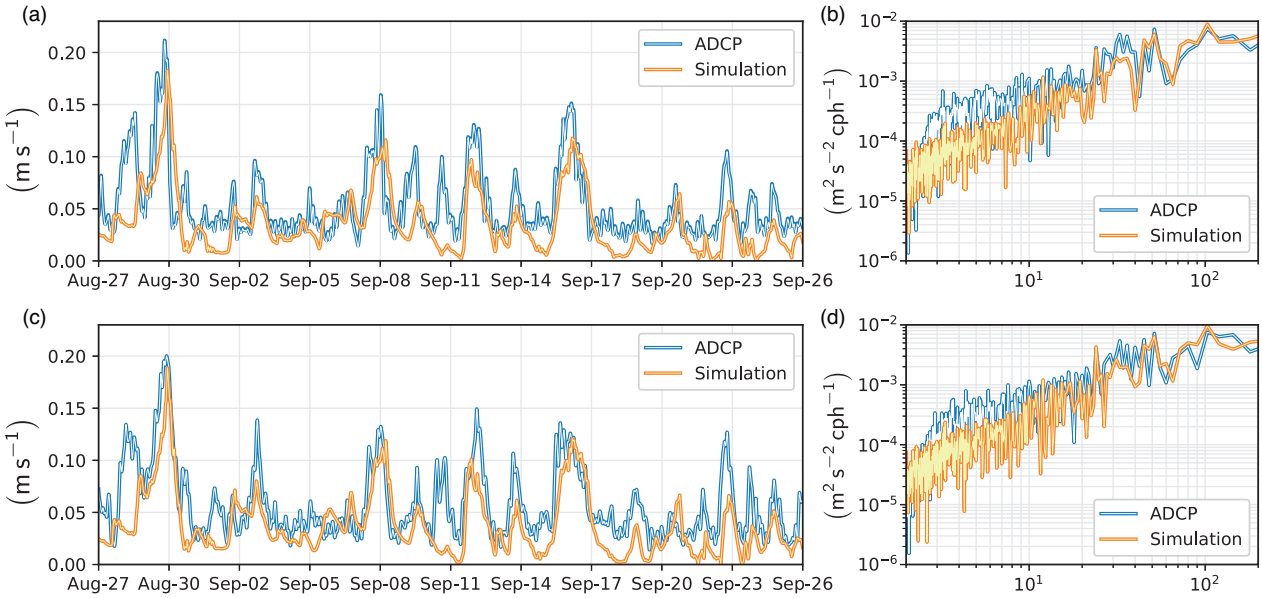

Figure 4: Time series of near-bottom velocity magnitude from ADCP (blue line) and numerical model (orange) at (a) Iansa Norte and (c) Iansa Sur for the winter period. See Figure 2(e). Panels (b) and (d) show the power spectra of the observed and simulated time series of the velocity magnitude in Iansa Norte and Iansa Sur, respectively; the horizontal axes in (b) and (d) denote periods in hours. The numerical model exceptionally reproduces the phase of the observed time series and the magnitude. Also, spectra reproduce low-frequency periods.

Figure 4 shows the time series of the near-bottom velocity magnitude from the ADCPs (blue lines) located in the areas called Iansa Norte and Iansa Sur, along with the time series of the numerical solution for the same variable in the nearest grid point (orange lines). In addition, Figure 4 provides power spectra for observed and simulated time series

for both sites. The results show that the numerically resolved near-bottom velocity magnitude is slightly lower than the observations. Overall, the model robustly reproduces the magnitude and phase of the ADCP observations. Appendix B reports a one-to-one model/observation comparison of the velocity components across the water column and their wavelet spectrum. We observe that the signal phase is better in winter than in summer. Yet, wavelet spectra show good coherence at low frequencies in both seasonal periods.

As an additional model's consistency check, we examine the lake thermal structure at the Campos et al. (1988) sampling station (Figure 2b), and we compare it to the scarce existing in situ data in Figure 3. Despite the above constraints, the model resolves the annual evolution of the temperature structure fairly well. Indeed, one of the critical features to reproduce is the thermal structure during the stratified period. Here, we observe that the numerical solution resolves both the temperature magnitude and the thickness of the surface mixed layer well. Moreover, the numerical model also reproduces the bi-annual CTD profiles taken in Lake Llanquihue during 2016 and 2017 (Supplementary Material A, Figure S.7). Last, we challenged the numerical model against the lake surface temperature inferred from MODIS satellite images. For a fair judgment, we compared the mean surface temperature derived from MODIS with the mean surface temperature obtained from the DELFT3D. The results show that the numerical model matches the annual trend of the mean surface temperature quite well (Supplementary Material A, Figure S.8). However, when the numerical model and MODIS results significantly differ, we cannot state that the numerical model is performing poorly. Indeed, we compared the temperature predicted from satellite images with the surface temperature obtained from the few CTD profiles we have access to. For example, the in-situ measured surface temperature for March 14, 2016, was 18.0°C. For the site where the CTD was cast, the numerical model predicted 17.7°C. For the same day, MODIS predicted surface temperatures ranging from 12.8° to 13.8°C over the lake area. Such a low temperature over the entire lake surface on a summer day is hard to justify. There is a substantial difference between MODIS temperature and in-situ observations and the model's result. The same mismatch occurred on March 14, 2017; the in-situ measured surface temperature was 18.1°C, and our model predicted 17.7°C at the sampling site. In contrast, MODIS results predict surface temperatures ranging from 13.4° to 13.8°. These differences might be due to cloudiness and sun glint, among other factors. Comparing numerical models and surface temperature inferred from satellite images requires in-situ validations and a critical assessment.

In summary, the calibrated numerical model reproduces processes with low frequencies, i.e., from seasonal timescales, such as lake thermal evolution, to nearshore currents at daily timescales. The latter makes the numerical model suitable for investigating the basin-scale hydrodynamics of Lake Llanquihue. Therefore, we do not examine processes occurring at time scales shorter than the inertial period, $T_f \approx 18.2$ h, such as trains of high-frequency internal waves and oscillations near the Brunt-Väisälä frequency, $N = \sqrt{-g\,\rho^{-1}\,\partial\rho/\partial z}$ (e.g. Lorke et al., 2006; de la Fuente et al., 2010; Dorostkar et al., 2017). However, we still characterize the spatiotemporal structure of the gravest superinertial internal Poincaré wave, whose period is marginally shorter than T_f. We report the basin-scale hydrodynamics of Lake Llanquihue in section 3.

2.5. *Modal analysis*

We investigated the basin-scale internal modes of motion following the modal analysis framework introduced by Shimizu et al. (2007). The pseudospectral modal analysis framework aims at solving the generalized eigenvalue problem,

$$\omega \, \mathbf{M} \, \tilde{\mathcal{A}} = \mathbf{K} \, \tilde{\mathcal{A}} \, , \tag{2}$$

which arises from seeking periodic wave solutions of the form $\mathcal{A}(\boldsymbol{x}, k, t) = \tilde{\mathcal{A}}(\boldsymbol{x}, k) \, e^{i \, \omega \, t}$ to the linearized equations of motion. Here, $\mathbf{M}$ and $\mathbf{K}$ are weight and external force matrices whose form depends on the background basin stratification and forcing terms. Thus, the problem reduces to computing the modal amplitudes $\tilde{\mathcal{A}}$, or eigenvectors, and the modal frequencies ω, or eigenvalues, that fulfill equation (2).

We investigated the spatiotemporal structure of internal modes of motion during the stratified season by considering a two-layer thermally stratified lake basin. These natural motions of a stratified lake are potentially energized by wind force, and they emerge in the system as basin-scale internal gravity waves. For the inviscid two-layer problem, the matrices $\mathbf{M}$ and $\mathbf{K}$ simplify to:

$$\mathbf{M} = \begin{pmatrix} \epsilon_1 \, g & 0 & 0 & 0 \\ 0 & \epsilon_2 \, g & 0 & 0 \\ 0 & 0 & h_1 & 0 \\ 0 & 0 & 0 & h_2 \end{pmatrix} \quad \text{and} \quad \mathbf{K} = \begin{pmatrix} 0 & 0 & \epsilon_1 \, g \, \nabla \cdot h_1 & \epsilon_1 \, g \, \nabla \cdot h_2 \\ 0 & 0 & 0 & \epsilon_1 \, g \, \nabla \cdot h_2 \\ h_1 \, g \, \nabla \epsilon_1 & 0 & 2 \, \boldsymbol{\Omega} \times h_1 & 0 \\ h_2 \, g \, \nabla \epsilon_1 & h_2 \, g \, \nabla \epsilon_2 & 0 & 2 \, \boldsymbol{\Omega} \times h_2 \end{pmatrix} , \tag{3}$$

where $\epsilon_1 = \rho_1 / \rho_2$ and $\epsilon_2 = (\rho_2 - \rho_1) / \rho_0$ are the dimensionless density differences across the surface and internal interfaces, respectively, with ρ_0 a reference value and g the gravitational acceleration. $\boldsymbol{\Omega} = (f/2) \hat{\boldsymbol{z}}$ is the local vertical angular velocity due to the Earth's rotation and f the Coriolis parameter, h_1 and h_2 are the upper and lower layers, respectively, whereas $\nabla = \partial_x \hat{\boldsymbol{x}} + \partial_y \hat{\boldsymbol{y}}$ is the two-dimensional horizontal gradient operator.

For the strongly stratified summer season, we resolved the two-layer eigenvalue problem numerically in a rectangular staggered mesh of square elements, considering an upper layer of thickness $h_1 = 30$ m, a lower layer thickness h_2 that depends on the lake topography, and a density difference between the bottom and surface layers of $\Delta\rho = 0.94$ kg m^{-3}. We also examined the winter conditions, considering the extremely weak stratification held by Lake Llanquihue. In winter, we identified an upper layer of approximately $h_1 = 60$ m and a density difference between the bottom and surface layer of about $\Delta\rho = 0.1$ kg m^{-3}. Here, we looked for the fundamental modes of the internal Kelvin and Poincaré gravity waves (e.g. Csanady, 1975; Antenucci and Imberger, 2001), which may store most of the wind-to-lake transferred energy (Gómez-Giraldo et al., 2006; Valerio et al., 2012; Fernández Castro et al., 2021).

2.6. *Tracer propagation and physical connectivity*

We employed the calibrated numerical model to examine the evolution of artificially released tracers in the water basin and thus determine their area of influence, trajectory, timescales, and, ultimately, the physical connectivity between strategically relevant zones along the littoral and across the water column.

Here, we perform two numerical experiments. In the first experiment, we use a conservative tracer governed by the transport equation:

$$\frac{\partial c}{\partial t} + \boldsymbol{v} \cdot \nabla c = \frac{\partial}{\partial x}\left(D_x \frac{\partial c}{\partial x}\right) + \frac{\partial}{\partial y}\left(D_y \frac{\partial c}{\partial y}\right) + \frac{\partial}{\partial z}\left(D_z \frac{\partial c}{\partial z}\right) + S(\boldsymbol{x}_0)\,. \tag{4}$$

where c is the tracer's concentration, $\boldsymbol{v}(\boldsymbol{x}, t)$ is the numerically integrated mean velocity field, D_r, with $r = x, y, z$, and are the tracer effective diffusivities (for each spatial component), i.e., the molecular diffusivity plus the numerically resolved turbulent diffusivity yielded by $k - \epsilon$ model, using the turbulent coefficients reported in Launder and Spalding (1974). S is a 'normal and linearly interpolated source term' (Deltares, 2014) that models a continuous discharge of the tracer at the coordinate $\boldsymbol{x}_0$. We use the source term to model a spill of a tracer in the littoral region, such as a near-surface discharge, to (i) track its evolution in space and time throughout the basin and (ii) examine the impact of the thermal cycle of the lake on its vertical distribution. Thus, equation (4) is integrated in time along with the heat and momentum equations.

In the second numerical experiment, we use neutrally buoyant Lagrangian tracers that have neither mass nor volume and fulfill the following evolution equation:

$$\frac{\mathrm{d}\boldsymbol{x}_p^{(n)}}{\mathrm{d}t} = \boldsymbol{v}(\boldsymbol{x}, t)\,. \tag{5}$$

Here, $\boldsymbol{x}_p^{(n)}$ corresponds to the position of the nth virtual particle and whose trajectory obeys only the deterministic advective transport driven by the RANS-resolved velocity field $\bar{\boldsymbol{v}}(\boldsymbol{x}, t)$. The position of the particle nth in a subsequent time Δt can be obtained by integrating (5):

$$\boldsymbol{x}_p^{(n)}(t + \Delta t) = \boldsymbol{x}_p^{(n)}(t) + \int_t^{t+\Delta t} \boldsymbol{v}\left(\boldsymbol{x}(\hat{t}), \hat{t}\right)\, \mathrm{d}\hat{t}\,. \tag{6}$$

Equation (6) is internally integrated using the model's time-step and the flow field resolved by DELFT3D-FLOW. The numerical method determines and uses the average velocity across the interfaces of the enclosed grid cells during the prescribed time step such that the grid cell fulfills mass conserving properties (continuity). The latter implies that the change in volume of the grid cell balances the sum of the flows across the interfaces during the time steps. Thus, the average velocity components are determined by the flows at each interface normalized by each interface area. The above assumption is thus consistent with a linear interpolation of the flow field, which can be analytically resolved, i.e., without numerical approximation, as shown in Postma et al. (2012). The entirely passive particles can be, then, conceptualized as tracers of individual water parcels (Cimatoribus et al., 2019). Thereby, given the initial particle conditions, we can track their streamlines (in space and time) and compute their deterministic pathways within the waterbody and their residence time, i.e., the time spent by particles in a given open volume.

Therefore, tracking passive particles allows investigating, in particular, the time and arc length, namely trajectory, taken by a water parcel to stream from one area to another. We coin this property as '*the physical connectivity*' between two regions, and it depends on time, the departure coordinate $\boldsymbol{x}_A$ and the destination coordinate $\boldsymbol{x}_B$, and the hydrodynamics, $\boldsymbol{v}$:

$$PC(t, \boldsymbol{x}_A, \boldsymbol{x}_B, \boldsymbol{v}) = [\tau_{A\to B}, \ell_{A\to B} \in \Omega]\,. \tag{7}$$

where $\tau_{A\to B}$ is the time taken by the particle to go from A to B and $\ell_{A\to B}$ is the trajectory followed by the particle to traverse from A and B, which can be approximated as:

$$\ell_{A\to B} \approx \sum_{j=1}^{m} \left\| \int_{t_0+(j-1)\,\Delta t}^{t_0+j\,\Delta t} \boldsymbol{v}\left(\boldsymbol{x}(\hat{t}),\hat{t}\right)\,\mathrm{d}\hat{t} \right\|, \tag{8}$$

with $\|\cdot\|$ the ℓ^2-norm, t_0 the initial time, Δt the integration timescale, and m the number of time steps needed by a particle to reach the destination. The complex dynamics displayed by the lake cause both the time $\tau_{A\to B}$ and the trajectory $\ell_{A\to B}$ to change as a function of time. Figure 5 illustrates the general pseudo algorithm used to compute the residence time and trajectory of particles that traverse a lake from A to B.

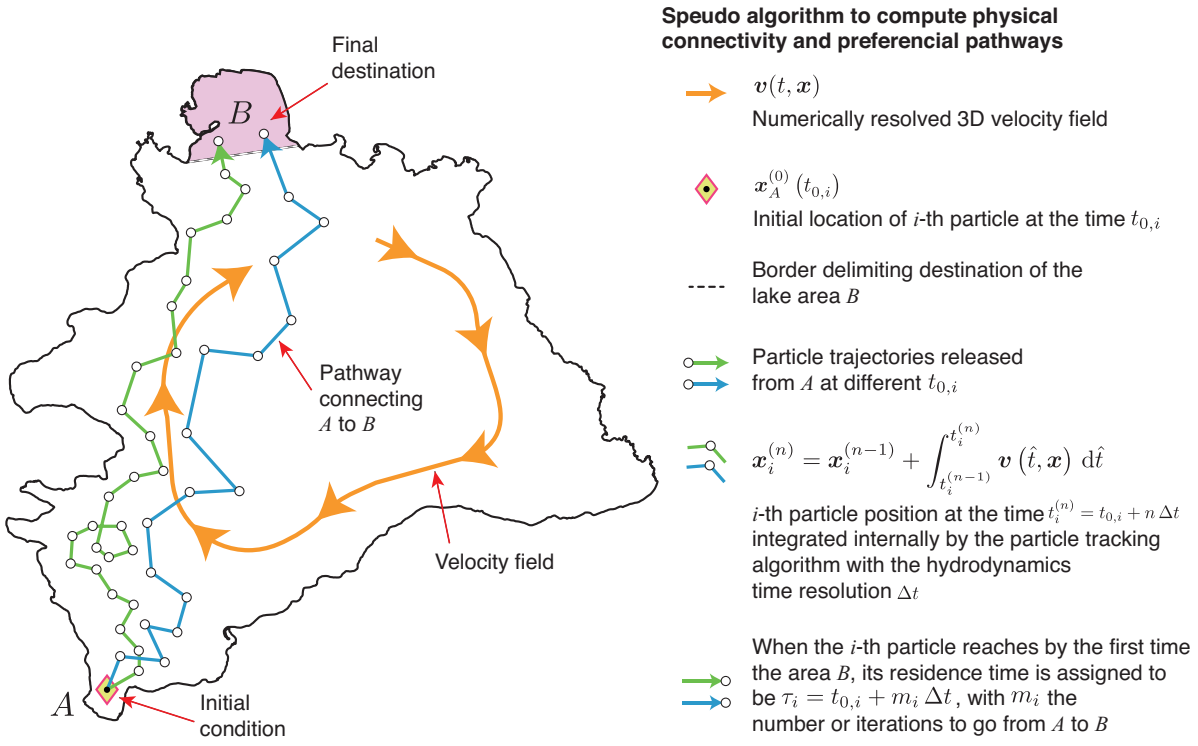

Figure 5: Pseudo algorithm used to examine residence time and particle trajectories connecting areas A and B.

However, one could consider the 'preferential pathway' followed by an ensemble of particles released at different times that move from A to B. We can thus approach the problem from a statistical viewpoint and obtain two fundamental metrics. First, the average time taken for water parcels to travel from A to B, $\bar{\tau}_{A\to B}$ over a certain period. Second, the most likely pathway $\bar{\ell}_{A\to B}$ that the hydrodynamics chooses to physically connect A and B. The latter requires assigning the residence time of a particle to all the cells included in a particular pathway. After repeating this process for all the particles that reached the final destination, we have a set of residence times for each cell's volume. Then, we calculate the average cell residence times to identify the preferential pathways and visualize the most likely path on a map. In section 4, we characterize the physical connectivity and preferential pathway between long-distance and strategically relevant nearshore zones in Lake Llanquihue. This information is instrumental for monitoring Lake Llanquihue and constitutes one of our main results.

3. Results: basin-scale hydrodynamics

We used the numerical model to identify persistent modes of motion at the basin scale and their potential relevance in enabling physical connectivity among urban and rural areas along Lake Llanquihue. Figure 6 shows the rotatory power spectral density (RPSD) for the velocity magnitude at a 35 m depth in the lake interior or pelagic zone, P1, and the lake nearshore, P2 (Figure 6a). The surveyed depth is above but close to the summertime metalimnetic zone and, therefore, ideal for investigating internal baroclinic and barotropic motions. The anticyclonic RPSDs for winter and summer in P1 are shown in Figure 6b and Figure 6c, respectively. Note that we display the RPSDs as a function of the period normalized by the inertial period. Consequently, super/subinertial periods are associated with sub/superinertial frequencies. We observe that most of the spectral energy is contained in near-inertial periods ($T/T_f \sim 1$) and periods longer than 100 h, both in winter and summer. In winter, the RPSD shows a bold energy peak at a subinertial 17.5 h period and two superinertial periods (subinertial frequencies) with significant peaks at approximately 205 h and 495 h. In summer, near-inertial periods contain more energy than in winter. The energy contained at superinertial periods also peaks at 205 h. Figure 6d and Figure 6e show the cyclonic RPSDs for the winter and summer seasons in P2, respectively. In contrast to cyclonic RPSDs, most of the spectral energy in anticyclonic flows is found at superinertial periods. In winter, we identify a distinctive high energy peak at 743 h (Figure 6d), whereas, in summer, the energy is stored at different superinertial periods, including 50 h, 144 h, 240 h, and 479 h (Figure 6e). However, the RPSD also shows a marked subinertial energy peak at 17.5 h. In the following subsections, we examine the basin-scale hydrodynamic processes of Lake Llanquihue and their link to the energy peaks identified in the RPSDs.

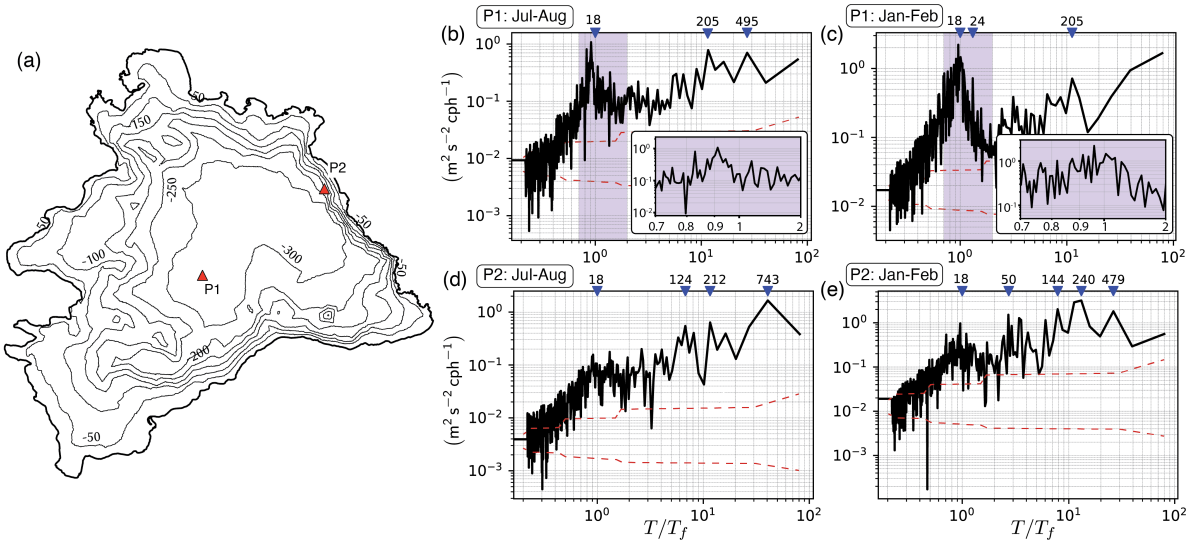

Figure 6: Panel (a) shows the sites in the lake interior (P1) and nearshore (P2) regions that we sampled numerically to examine the rotary power spectral density (RPSD) of the velocity magnitude at a 35 m depth. (b) Anticyclonic RPSD at P1 during winter (July to August of 2016) and (c) summer (January to March 2016). Cyclonic RPSD at P2 during (d) winter and (e) summer. Triangles on top of each RPSD panel denote periods close to the largest energy peaks. The inertial period at the lake latitude is $T_f \approx 18.2$ h. Dashed lines represent 95% confidence interval.

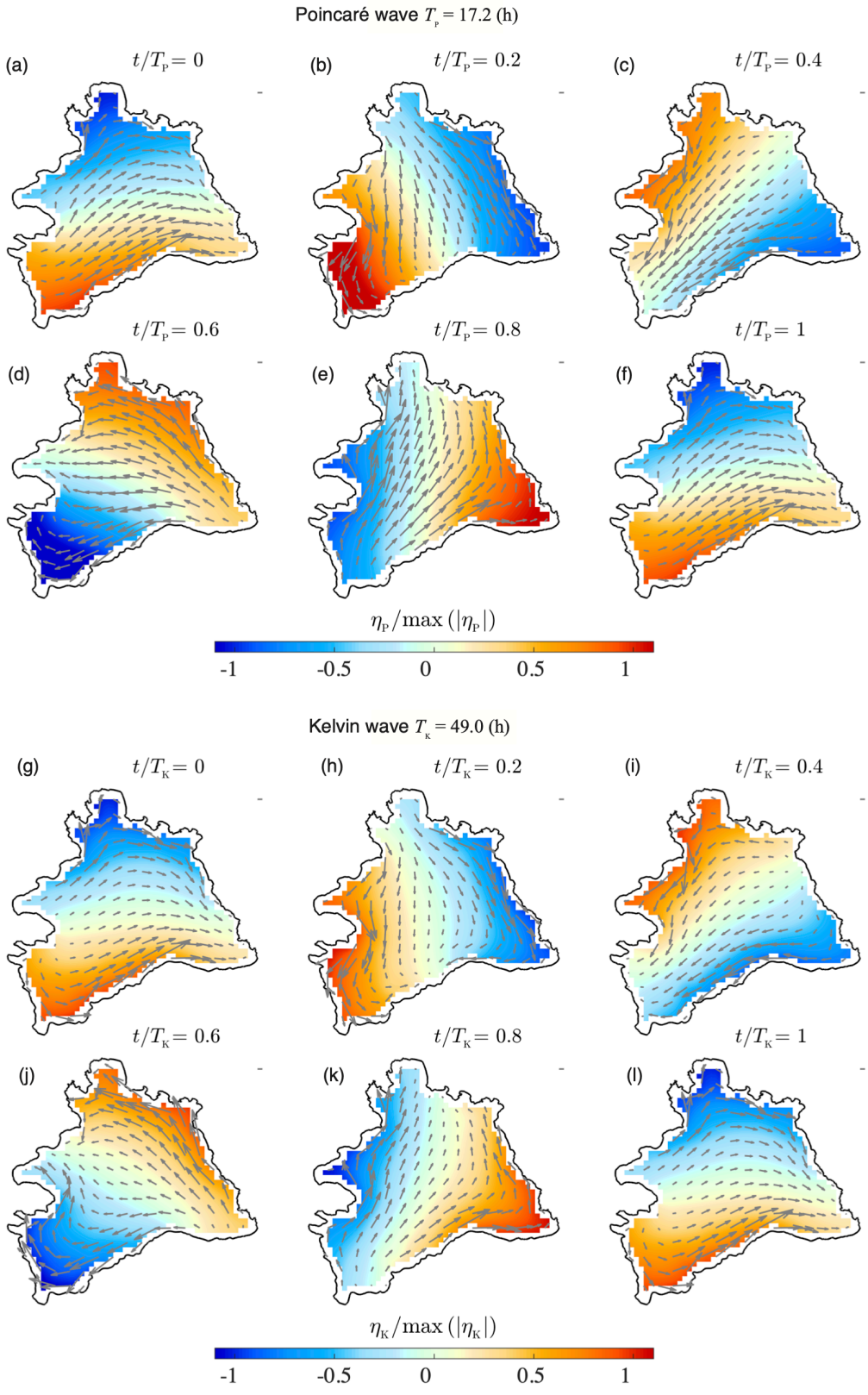

Figure 7: Results of modal analysis. Gravest internal modes of the Poincaré wave and Kelvin wave for the stratified period (January to March).

3.1. Natural modes of motion

Figure 7 shows the spatiotemporal evolution of the gravest, basin-scale internal modes associated with the 'summer' Poincaré and Kelvin waves, respectively. Panels show the horizontal modal structure of the normalized interface vertical displacement and the upper layer velocity field. The internal Poincaré wave shown in Figure 7(a-f) has a modal period of T_P = 17.2 h (superinertial frequency). Its upper layer propagates anti-clockwise, with maximum velocity magnitudes in the lake's center. In contrast, the largest vertical displacements of the interface η_P are found near the shore. Therefore, the energy peaks identified in the pelagic zone of Lake Llanquihue of approximately 17.5 h period, shown in Figure 6(c), can be associated with the gravest internal Poincaré mode. In contrast, the internal Kelvin wave shown in Figure 7(g-i) has a modal period of T_K = 49 h (subinertial frequency). Its upper layer propagates clockwise, and its velocity field and interface displacement η_K exhibit exponential decay from the coast to the lake interior. Thus, the spatiotemporal structure of this mode of motion explains the energy peak of approximately 50 h period observed in the littoral zone, shown in Figure 6(e).

In the weakly stratified winter, the Kelvin wave has a theoretical period of 129 h (subinertial frequency). In contrast, the Poincaré wave has a period of 17.4 h (superinertial frequency). Note that the Poincaré wave has almost the same period as that in summer; its frequency converges asymptotically to the inertial frequency as the Burger number decreases (Antenucci and Imberger, 2001). The RPSD computed from the numerically resolved nearshore velocity field in winter (Figure 6d) exhibits a marked energy peak at approximately 124 h. This peak in energy could be attributed to the presence of wintertime Kelvin waves, a mode of motion scarcely studied in the literature. Similarly, the RPSD computed in the pelagic zone for the winter period (Figure 6b) also exhibits a high energy peak at the near-inertial period. This energy peak can be attributed to the wintertime Poincaré wave activity.

3.2. Circulation pattern and gyres

We characterized the general horizontal circulation of the upper and mid-depth water column utilizing the numerically resolved three-dimensional velocity and temperature fields resulting from the atmospheric forcing between October 2015 and January 2017. The large-scale circulation in Lake Llanquihue is characterized by closed-loop current patterns, known as gyres, that persist through the seasons.

The vertically-averaged, upper water circulation spans depths between 4 and 37 m to capture the basin-scale flow pattern within the seasonal epilimnetic region without integrating the direct influence of diurnal variations in the surface waters. Figure 8 shows three physical variables: first, the monthly averaged, upper depth-averaged horizontal velocity field (arrows); second, the horizontal spatial distribution of the temperature field at a 37 m depth; and third, the monthly direction and magnitude of wind distribution at the center of the lake. The most prominent and persistent feature observed in the upper waters of Lake Llanquihue is a large-scale cyclonic (clockwise) gyre. Its 'eye' is roughly centered on the lake's northeast side, where the deepest waters are found (Figure 2b).

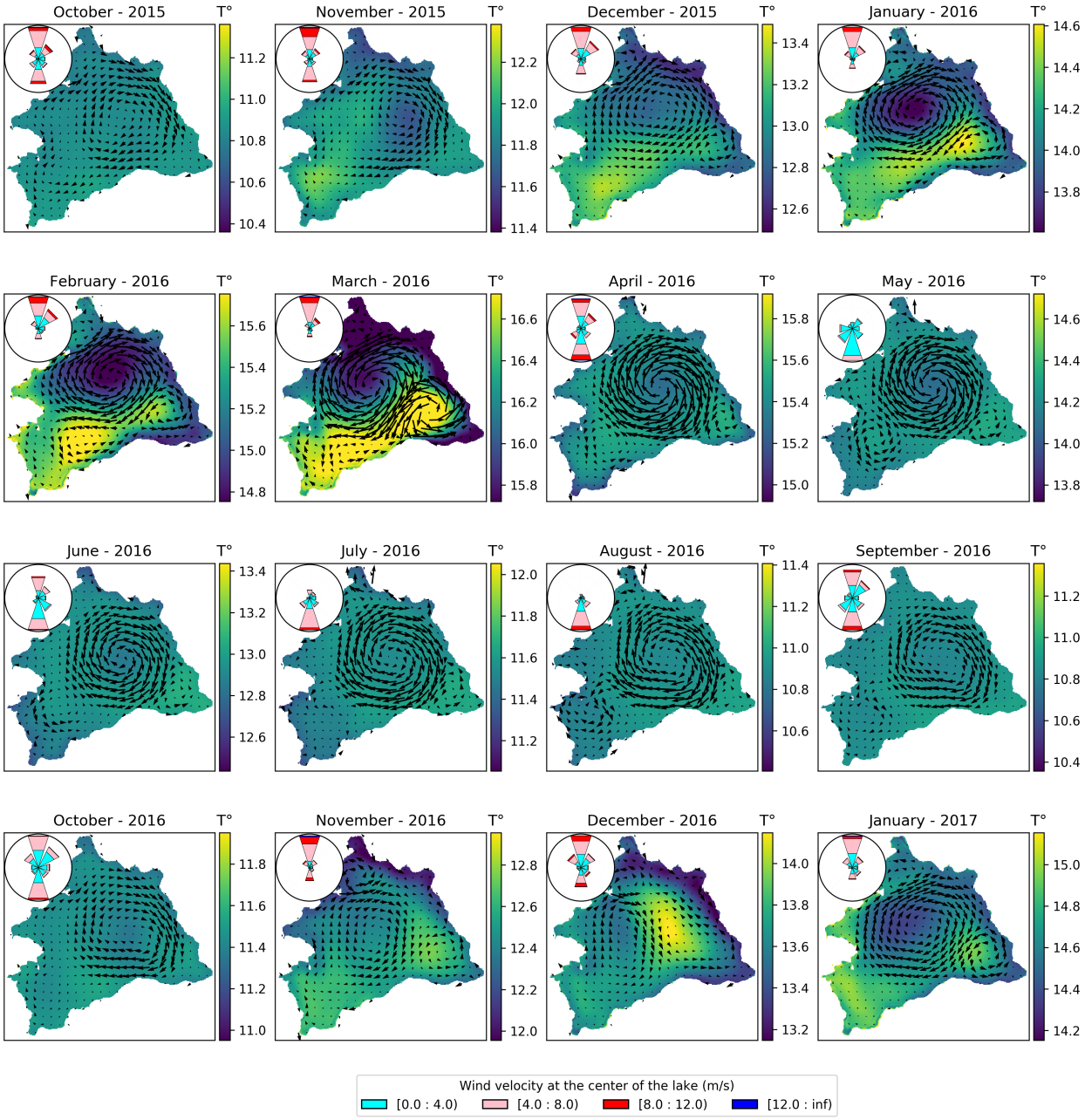

Figure 8: Monthly mean circulation pattern between 4 and 37 m depth, superimposed on water temperature at 37 m. Each panel shows the wind rose for the interpolated wind at the lake center.

When the lake gains heat and becomes strongly stratified from January to March 2016 (Figure 3f-h), the upper layer horizontal velocity field increases in magnitude. Figure 8 shows that during the austral summer, the centre of the large-scale cyclonic (LSC) gyre is associated with the upwelling of cold deep waters to the upper layer. At the same time, we also identify the formation of a mesoscale anti-cyclonic (MAC) gyre in the eastern region of the basin near Ensenada. The MAC gyre is associated with the downwelling of warm surface waters to deeper zones. The coexistence of the LSC gyre in the northern region and the MAC gyre in the eastern part drives a massive upwelling on the east

littoral zone, causing a maximum temperature drop in March 2016. This littoral upwelling also correlates with the formation of a pool of warm waters over the southwestern region of the basin. The above temperature and flow features in the upper lake waters start to change with the beginning of the cooling seasons–autumn and winter–from April to September 2016. During the cooling period, the signature of the cold, upwelled waters at the eye of the LSC gyre decays progressively. In contrast, the pool of warm waters associated with the MAC gyre and its circulation pattern vanish entirely. From May to September 2016, a weak yet distinguishable anti-cyclonic circulation emerges in the grand bay of Puerto Varas and Llanquihue.

At mid-depths (e.g., between 62 m and 79 m), within hypolimnetic waters, the horizontal lake area has yet to be dramatically reduced due to the sloping bathymetry. Here, the horizontal flow reveals a progressive formation of a basin-scale cyclonic current from November (2015) to March (2016) that streams along the lake perimeter. Its size, however, starts shrinking from April to September. Although its horizontal location coincides with the position of the LSC gyre observed in upper waters (Figure 8), the horizontal velocity field has magnitudes lower than those near the surface. No coherent MAC gyre is identified at this mid-depth zone in the eastern basin near Ensenada. These results suggest that the MAC gyre is an upper localized circulation pattern. In contrast, the LSC gyre takes place over a substantial part of the water column during the cooling season (Figure S.5, Supplementary Material A).

Our results show that Lake Llanquihue hosts two wind-driven and predominant circulation patterns over the seasons. The main circulation feature is characterized by a large-scale cyclonic gyre, whose eye is near the lake's center. In winter, its outer radius is $R_{\mathrm{LSC}} \approx 10.34$ km and mean orbital speed of 2.4 cm s^{-1}, whereas in summer $R_{\mathrm{LSC}} \approx 9.87$ km and the mean orbital speed is 3.5 cm s^{-1}. The above metrics of the LSC gyre lead to orbital periods of 752 h in winter and 492 h in summer. The second circulation feature is a mesoscale anticyclonic gyre localized towards the eastern side of the basin. In winter, its outer radius is $R_{\mathrm{MAC}} \approx 4.5$ km and mean orbital speed of 3.0 cm s^{-1}, whereas in summer $R_{\mathrm{MAC}} \approx 4.3$ km and the orbital speed is 3.5 cm s^{-1}. Thus, its orbital periods for winter and summer are 227 h and 251 h, respectively. The magnitude of the orbital periods estimated for the LSC gyre and the MAC gyre is consistent with the periods of the gravest power spectral energy peaks shown in Figure 6. The coupling effect of these two gyres leads to the upwelling of cold water in the northeastern basin and warm waters in the southwestern basin.

4. Results: Tracer experiments and physical connectivity

4.1. Conservative tracer experiments

We first examine the basin-scale propagation of a conservative tracer spilled from three main cities settled by the western lakeshore, Puerto Varas, Llanquihue, and Frutillar (Figure 2b). Here, however, we only focus on the results from Puerto Varas–the largest city in the lake's catchment. For completeness, results from Llanquihue and Frutillar are provided in Supplementary Material A. The flow rate of the tracer was set proportional to each city's population to simulate a 'potential' sewage water discharge released 130 m offshore of each location at the uppermost 'hydrodynamic layer', i.e., between the surface and about 1 m depth. The tracer was spilled for a year from August 2016 to August 2017, and its concentration was tracked over time at six observation points around the lake's nearshore region. We also measured mean concentration at two different zones in the water column, in epilimnetic waters, $-36.6\,\mathrm{m} \leq z \leq 0\,\mathrm{m}$,

and upper hypolimnetic waters found beneath the strongly stratified zone in the summertime, $-78.9\,\mathrm{m} \leq z \leq -62.6\,\mathrm{m}$. The latter two controlling zones allowed us to identify periods under which the vertical exchange between surface and deep waters is diminished or enhanced.

Figure 9 shows numerical results of the tracer released from Puerto Varas. The central panel (g) illustrates the shoreline of Lake Llanquihue, and indicates the discharge site (red circle) and the observation points on the lake area (crosses). Each observation point is labeled (A-F) and linked to a panel that exhibits the tracer concentration normalized by the maximum concentration observed in the discharge system, $c/c_{\max}$, in the vertical axis as a function of time (horizontal axis) for both the epilimnion (red curve) and hypolimnion zones (blue curve). The general trend exhibited by the time series (and in all the sites) are described next.

Initially, epilimnion and (upper) hypolimnion concentrations increase simultaneously, following close magnitudes. The latter is owing to the well-mixed water column that initially receives the tracer in Winter. However, as winter ends and spring progresses, the concentration in epilimnetic waters takes off, whereas the concentration in the hypolimnion decays over time until reaching a plateau. Thus, the concentration difference between the epilimnion and hypolimnion grows continuously throughout the stratified summertime, reaching a peak in late summer. The above is due to an increase in the epilimnion concentration, resulting from the severe decline of the vertical exchange during the thermally stratified season. For the same period the concentration in hypolimnetic waters remains fairly uniform until the cooling period begins. During the cooling seasons, i.e., autumn-winter, the tracer's concentration in the hypolimnion rises exponentially because of vigorous vertical mixing resulting from thermal convection. The annual cycle closes when the epilimnion and hypolimnion concentrations converge in mid-winter, indicating that a new deep mixing period started in Lake Llanquihue. A general characteristic, but expected, is that the maximum concentration is always found in the vicinity of the discharge area.

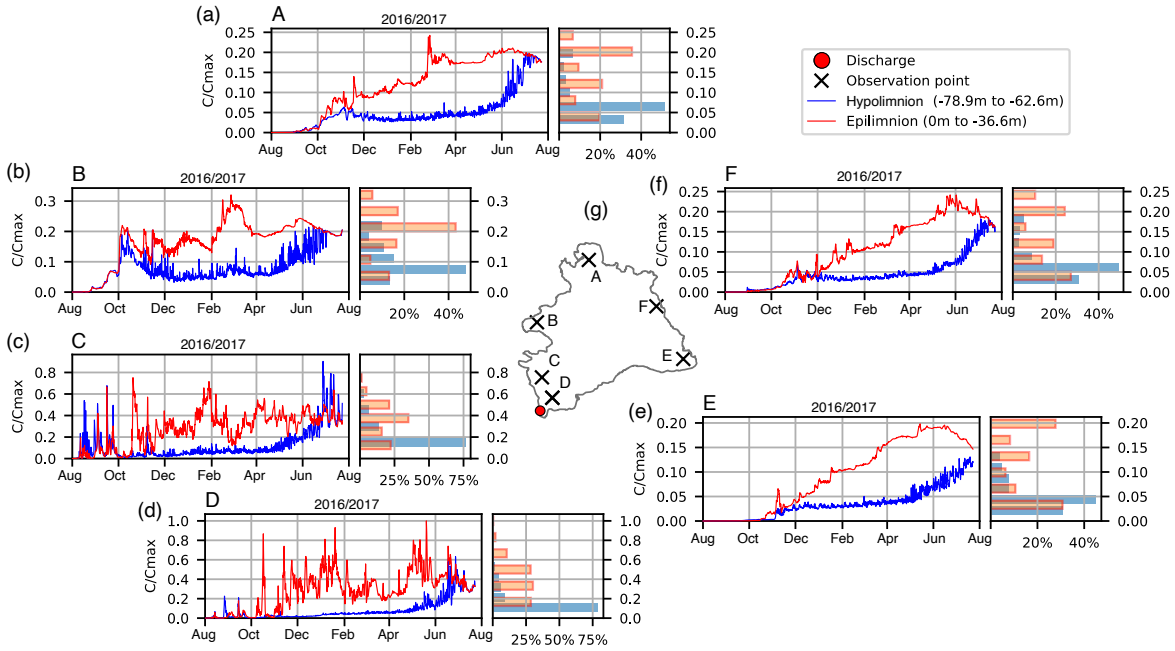

Figure 9: Numerical model results: Tracer experiment for 08/2016-08/2017. Crosses denote numerical monitoring points for the tracer released from the littoral zone of Puerto Varas (red circle). Panels show time series of the normalized tracer concentration $c/c_{\max}$ at each location. Red lines denote $c/c_{\max}$ within the surface waters, 0-36.6 m, whereas blue lines denote $c/c_{\max}$ for deep waters, 62.6-78.9 m. Note that the scale for $c/c_{\max}$ may change from panel to panel. Along with each time series, we show histograms of the normalized concentration for both zones in the water column to illustrate their modal distribution.

In contrast to the global trends, at short (daily) timescales, each releasing (and measuring) site exhibits unique local dynamics. Figure 9d shows the concentration evolution in the nearest observation point to the discharge in Puerto Varas. The concentration measured at the remainder of the observation points (C-B-A-F-E) decays in the clockwise direction, and their peaks over time suggest that a cyclonic basin-scale circulation advects the tracer along the lake's littoral region. The concentration in the nearest observation points (D-C-B) reveals high oscillations in the epilimnion. In the case of the narrow bay of Frutillar (Figure 9b), the concentration exhibits particularly large oscillations over time. Interestingly, during the winter period, concentrations in the hypolimnion tend to be larger than those in the epilimnion. This phenomenon, also observed in the shallow regions along the southwest littoral zone, is associated with autumn-winter south winds that can support Ekman-driven downwelling along the west coastline. In contrast, at the furthest observation points (A-E-F), the epilimnion concentration grows almost linearly over time, especially at the monitoring points along the eastern side of the lake. At these furthest points, and after ten months, the concentration reaches up to 20% of the initial concentration observed in Puerto Varas. Unlike the tracer's evolution from the other discharge sites, a discharge from Frutillar generates equally low concentrations at the observation points (see Supplementary Material A, S.10 for further information). The peak in concentration observed at each point suggests that the tracer is cyclonically transported from Frutillar (B) to the rest of the littoral measuring points (A-F-E-D-C). In particular, we note that regions

near Puerto Varas (D) and Llanquihue (C) present no concentration for more than three months.

Table 2 summarizes the maximum concentration observed in the epilimnion (EMC) and hypolimnion (HMC) at each observation site and the number of days between the first maximum and the start of the tracer discharge (day_{EMC}, day_{EMC}). We found that the discharge from the 'bay of Frutillar' exhibits a limited exchange with the rest of the littoral zone, where less than 8% of the maximum concentration is registered over a year. The discharge from Llanquihue's area, on the other hand, shows a significant impact along the littoral region of the lake. Indeed, all the observation points reach more than 20% of the maximum concentration measured in the vicinity of Llanquihue. The significant contrast between discharge footprints in Frutillar and Llanquihue and the rest of the nearshore regions can be well understood by examining the large-scale circulation pattern in these areas. In the case of the bay of Frutillar, the persistent LSC cyclonic running around the main basin (Figures 8 and S.5) does not reach the most sheltered area of the bay, precluding its efficient ventilation. In contrast, the littoral region of Llanquihue is found in the circuit of complex currents of slightly higher magnitude than those observed within the bay of Frutillar. In autumn (April-June), a local mesoscale anti-cyclonic gyre transports the tracers towards the bay of Puerto Varas. The latter circulation pattern supports having a high tracer concentration measured in the bay of Puerto Varas, whereas the rest of the year, a mesoscale cyclonic gyre transports the tracer towards the north, feeding the western side of the LSC gyre hosted in the pelagic region of Lake Llanquihue.

Table 2: Metrics associated with the tracer discharge shown in Figures 9, and Figures S.9 and S.10 in Supplementary Material A. EMC and HMC are the epilimnion and hypolimnion maximum concentrations, reached day_{EMC} and day_{HMC} days after the discharge began.

Observation point	**Discharge from:**		
Labels in Figure 9 and Figures S.9 and S.10	Puerto Varas (EMC% | HMC%) (day_{EMC} | day_{HMC})	Llanquihue (EMC% | HMC%) (day_{EMC} | day_{HMC})	Frutillar (EMC% | HMC%) (day_{EMC} | day_{HMC})
Puerto Varas (D)	100% | 63% 292 | 330	100% | 48% 187 | 320	8% | 6% 241 | 335
Llanquihue (C)	75% | 90% 80 | 330	100% | 100% 227 | 351	8% | 6% 323 | 336
Frutillar (B)	32% | 22% 209 | 317	48% | 29% 217 | 317	100% | 73% 246 | 345
Puerto Octay (A)	24% |20% 209 | 336	36% | 25% 207 | 336	6% | 5% 74 | 318
Las Cascadas (F)	24% | 18% 296 | 347	32% | 23% 293 | 347	7% | 4% 289 | 337
Ensenada (E)	20% | 13% 286 | 352	26% | 16% 286 | 352	5% | 3% 295 | 352

4.2. Physical connectivity and preferential pathways

We investigate the basin-scale propagation of neutrally buoyant Lagrangian particles (hereafter just particles) released from the three major cities studied in the last subsection and two rural locations with a growing tourism-based economy linked to Lake Llanquihue–Puerto Octay and Ensenada (see Figure 2b). Table 3 summarizes the coordinates from where particles were released from the uppermost 'hydrodynamic layer' into the lake and the periods considered to analyze the physical connectivity amongst the abovementioned littoral areas. Here, however, we focus on examining tracers' propagation from three locations, Puerto Varas, Puerto Octay, and Ensenada, which represent extreme geographical zones within the lake (Figure 2b). For the sake of completeness, results from Llanquihue and Frutillar are provided in Supplementary Material A.

Table 3: Coordinates and dates of Lagrangian particle release.

Location (Nearest town)	**Coordinates** (Lat-Lon)
Puerto Varas	41°19'08"-72°57'58"
Llanquihue	41°15'11"-72°59'19"
Frutillar	41°08'04"-73°01'06"
Puerto Octay	40°58'26"-72°52'10"
Ensenada	41°12'21"-72°32'53"

Season (Southern Hemisphere)	**Start-End Dates** (mm/dd/yyyy)
Autumn-Winter (AW)	06/01/2016-09/01/2016
Spring-Summer (SS)	12/01/2016-03/01/2017

Figures 10-11 (and S.11 and S.12 in Supplementary Material A) illustrate the average time taken by particles to stream from a release point (colorbar in day unit), denoted by a black diamond, to a specific area in the littoral, shaded white and marked by a magenta star. Each figure is compounded by eight panels. Four panels (left side) map the autumn-winter (AW) conditions, whereas the other four (right) map the spring-summer (SS) conditions. White spots not linked to magenta stars (mainly in the lake interior) denote areas where no particles are identified over the periods considered for the Lagrangian numerical experiments. Additionally, not all the particles must reach the 'destination zone' in the period under study. Pinkish colors denote shorter times to flow from zone A to zone B, whereas bluish colors denote longer times. Thus, areas on the lake that share a specific color provide qualitative information on the preferential pathways that particles stream (on average) from one specific location to another. For instance, Let us consider the results shown in Figure 10a. In this case, particles are released from the bay of Puerto Varas (black diamond), and the target destination is an area in the littoral waters of Llanquihue (magenta star) during the autumn-winter period. We observe continuous colors bridging both areas. In particular, very near the shoreline, we identify (pinkish colors that denote) fairly straight trajectories of particles that take approximately 19 days to travel from Puerto Varas to Llanquihue littoral waters. In some cases, however, it is indeed hard to identify a continuous, single-color area connecting two regions. As an extreme case, see Figure 10h; it illustrates the connectivity between Puerto Varas (black diamond) and Ensenada (magenta star). Note that for each Lagrangian numerical experiment, we can always compute the shortest traveling time taken by a particle to stream between two regions. We next describe the most distinctive preferential pathways through which particles choose to stream from one site to another in the shortest time across Lake Llanquihue.

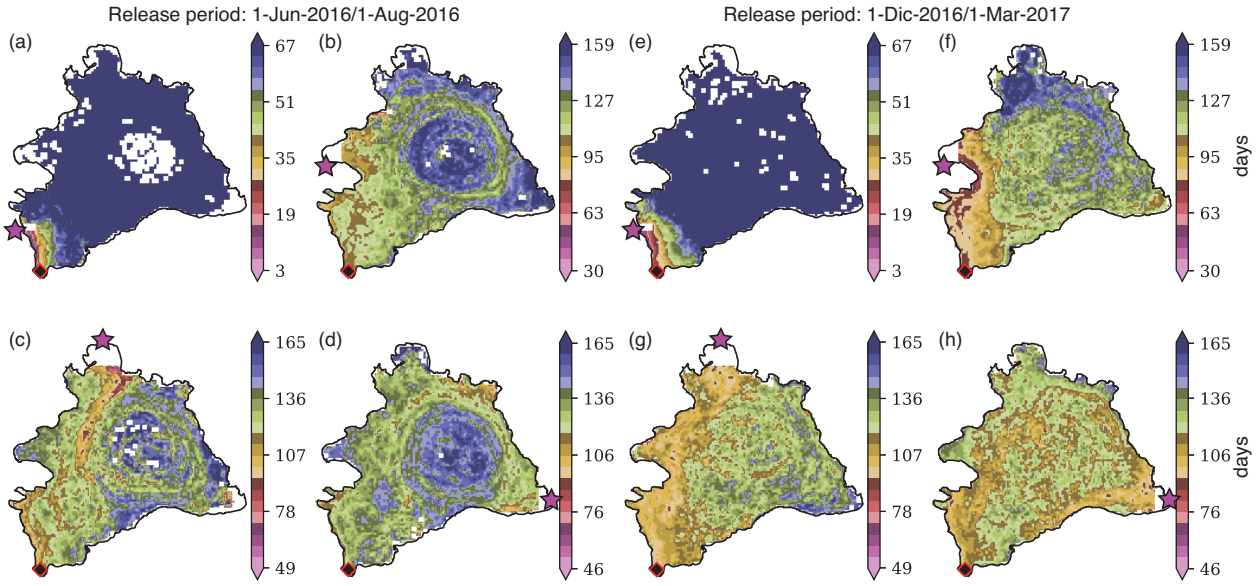

Figure 10: Lagrangian tracer analysis: maps of the mean residence time and preferential pathways throughout Lake Llanquihue.Left panels show results from the autumn-winter (AW) season (Jun-1-2016/Aug-1-2016), whereas right panels show results from the spring-summer (SS) season (Dec-1-2016/Mar-1-2017). The colorbar in day units denotes the time taken by Lagrangian tracers released from Puerto Varas to reach the nearshore region of (a,e) Llanquihue city, (b,f) Frutillar city, (c,g) Puerto Octay town, and (d,h) Ensenada town.

Particles streaming to Llanquihue and Frutillar follow the western shoreline in the AW and SS periods. To get to Puerto Octay's bay, particles stream along the basin's western side current. In the case of the SS season (Figure 10g), particles occupy a rather wide area (Figure 10c). In winter, however, the preferential pathway is narrower and initially confined to the nearshore region, yet particles detach from the littoral near the bay of Frutillar, from which they stream following the local trajectory of the LSC gyre. To reach the furthest area, Ensanada (10d,h), particles stream following the cyclonic trajectory set by the LSC gyre characterized in Figure 8.

The relevance of the LSC gyre as a critical mechanism to physically connect long-distance zones is boldly shown in Figure 11. This figure characterizes the time taken by particles to travel from Ensenada to Puerto Varas (panels a and e), Llanquihue (panels b and f), Frutillar (panels c and g), and Puerto Octay (panels d and h). The particles stream throughout the southern pelagic waters in the AW season (11a,b) to get to Puerto Varas and Llanquihue, whereas in the SS season, they stream close to the shoreline (11e,f). To reach Frutillar and Puerto Octay, particles profit from the LSC gyre circulation, strikingly imprinted in their AW season pathway towards Puerto Octay, as shown in Figure 11d.

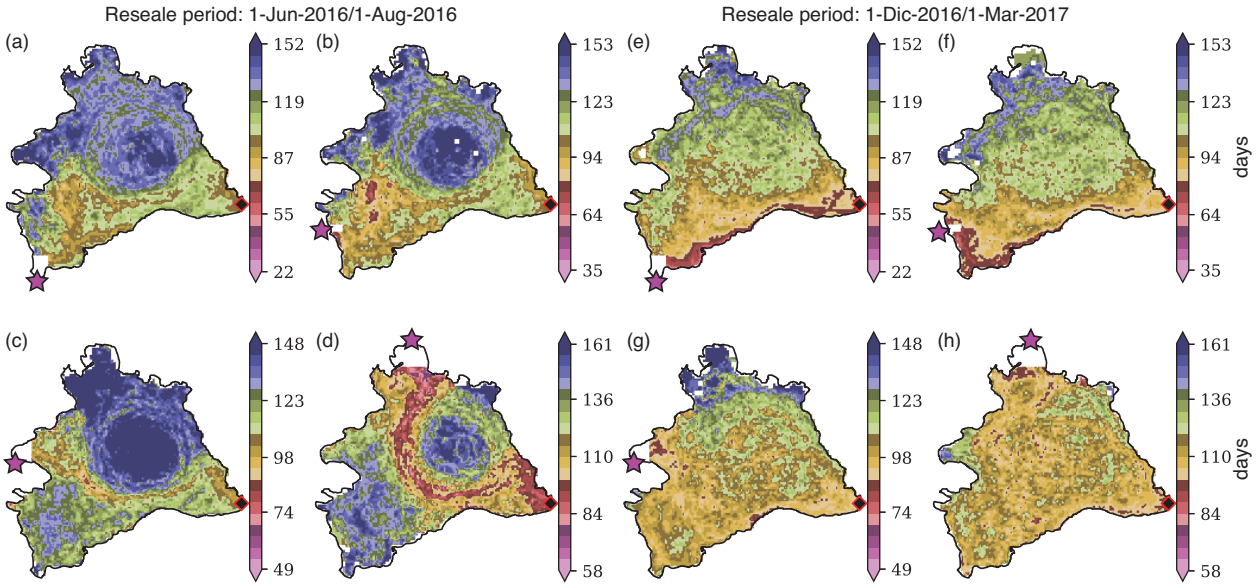

Figure 11: Lagrangian tracer analysis: maps of the mean residence time and preferential pathways throughout Lake Llanquihue. Left panels show results from the autumn-winter (AW) season (Jun-1-2016/Aug-1-2016), whereas right panels show results from the spring-summer (SS) season (Dec-1-2016/Mar-1-2017). The colorbar in day units denotes the time taken by Lagrangian tracers released from Ensenada to reach the nearshore region of (a,e) Puerto Varas city, (b,f) Llanquihue city, (c,g) Frutillar city, and (d,h) Puerto Octay town.

Table 4 summarizes the average traveling time taken by particles to stream from one nearshore site to another, both in the autumn-winter (AW) season and spring-summer (SS) season. Note that particles streaming from the site A to site B have different preferential pathways and timescales to particle streaming in the opposite direction, i.e., from B to A. Our results show that particles can take between two and four months to travel from one site to another around the lake littoral zone. In particular, we found that, in the SS season, particles reach their destinations in shorter times than in the AW season. During the former period, particles become more confined within the upper surface mixed layer by the effect of thermal stratification, limiting their potential three-dimensional trajectories.

Table 4: Number of days taken to connect physically different areas along the lake's littoral, in autumn-winter (first number) and spring-summer (second number) seasons.

From / To	LLanquihue	Frutillar	P. Octay	Ensenada	P. Varas
Llanquihue	·	90.3 / 92.5	84 / 71	107.4 / 90.3	98.2 / 92
Frutillar	90.3 / 92.5	·	84 / 71	107.4 / 90.3	98.2 / 92
P. Octay	101.3 / 88.8	110.8 / 93.2	·	78.2 / 73.4	101.2 / 86.6
Ensenada	93.4 / 79	100.3 / 89.6	86.5 / 99.2	·	91.7 / 66
P. Varas	19.2 / 22.1	99.3 / 76.8	103.9 / 98.2	120.8 / 101.5	·

5. Discussion

5.1. Llanquihue, a Patagonian lake

Patagonia is an intriguing hotspot of surface freshwater on Earth. After the last deglaciation, depressions, shaped by the retreat of glaciers and a tortuous Andes mountain range, were covered by lakes. Yet the number of lakes in this region is constantly increasing due to the pervasive retreat of the ice fields of southern Patagonia (Willis et al., 2012; Mouginot and Rignot, 2015). Although these water bodies are still assumed pristine, little is truly known about them–we can only validate such an assumption with field studies. This paper reports the hydrodynamics of Lake Llanquihue, a northern Patagonia lake found in the so-called lakes district zone. The increasing human development experienced in this zone is not being followed by a comprehensive evaluation of the lakes' physical and biogeochemical state. Some of these freshwater bodies are already experiencing symptoms of eutrophication faced more than four decades ago by Northern lakes. Therefore, it is essential to transfer knowledge and learn from the challenges and trophic pathways followed by Northern lakes. Most importantly, it is crucial to establish baselines and monitoring programs and develop policies that protect and ensure the health of Patagonian lakes and their sustainable use.

Developing the present study for Lake Llanquihue was challenging owing to the scarce, discontinuous and scattered existing data. To set the thermohydrodynamic numerical model, we utilized atmospheric data from a network of weather stations found in the vicinity of the lakeshore. As a base thermal state, we assumed the only available monthly resolution annual temperature data reported by Campos et al. (1988) more than three decades ago. We expanded the dataset by integrating the temperature profiles collected by the Lake Llanquihue monitoring program led by DGA, the Chilean Division of Water Resources, during the studied period 2015-2017. The latter period was chosen because we had access to short-term ADCP observations measured by the DOP, the Chilean Division of Port Works. These limited field measurements enabled us to calibrate and critically assess the observations and the numerical results. Undoubtedly, more robust numerical models might be achieved with denser in-situ data and well-designed field campaigns. This study encourages new research and fieldwork expeditions to measure the temperature evolution, currents in the littoral and pelagic waters, and atmospheric forcing on Lake Llanquihue. Future physical studies should be preferentially designed and executed in parallel with biochemical studies to examine the intimate relationship between the lake thermohydrodynamics and the distribution of nutrients, biomass, and dissolved gasses.

5.2. Basin-scale modes of motion

Winds blowing on Lake Llanquihue have a remarkable circadian rhythm of 24 h, especially during the Austral summer (Figure S.3b), which energizes a wide range of motions. Here, we investigated those motions governing the basin-scale hydrodynamics responsible for long mass excursions within Lake Llanquihue. Given the lake's size, stratification, and latitude, the basin-scale internal motions are affected by Coriolis acceleration. The stratified summer period has a Burger number (Antenucci and Imberger, 2001) $\mathcal{B} \approx 0.3$, supporting the existence of a wide range of internal waves frequencies, from superinertial frequencies, with periods shorter than $T_f \approx 18.2$ h, to subinertial frequencies, with periods of several days.

Here, we characterized the basin-scale internal Kelvin and Poincaré waves (Csanady, 1975). From the summer density stratification, we expected the gravest anti-cyclonic Kelvin mode to have a period of approximately 49 h (Figure 7g-l), which was confirmed by the rotatory power spectral density (RPSD) (Figure 6e) obtained from velocity field time series. This wave period is near twice that of the gravest internal Kelvin wave observed in the neighboring Lake Villarrica (Rozas et al., 2014) and almost half the period of the internal Kelvin wave reported in Lake Geneva (Bouffard and Lemmin, 2013) during the boreal summer. Although not investigated in this study, the aspect ratio of the thermal stratification in Lake Llanquihue, i.e., the ratio between the thermocline depth and the mean depth $h_t/h_m \approx 0.22$ (see Table 1), supports a degenerative process that can affect the evolution of internal Kelvin waves (de la Fuente et al., 2008; Sakai and Redekopp, 2010; Ulloa et al., 2014) and lead to the formation of solitary-type waves of depression (de la Fuente et al., 2010; Dorostkar et al., 2017) and supercritical shear flows at metalimnetic depths (Preusse et al., 2012; Ulloa et al., 2015). In contrast, the gravest internal Poincaré wave has a cyclonic propagation and a period of approximately 17.2 h in Lake Llanquihue (Figure 7a-f) and has its maximum modal amplitude in the lake interior. Yet, it can still imprint its signature near the littoral region, as shown in the RPSD in Figure 6c,e. Shear-induced by Poincaré waves can drive Kelvin-Helmholtz billows, enhance vertical mixing in the pelagic pycnocline region (Bouffard et al., 2012; Choi et al., 2012), and lead to resuspension and turbidity episodes in zones where the pycnocline interacts with the lake bed, as identified in Lake Erie (Valipour et al., 2017; Lin et al., 2021).

In addition, the numerical results show that Lake Llanquihue is densely populated by inertial waves. These waves have orbital motions of length scale $\ell_f \sim U/f \approx 3$ km that store significant kinetic energy both in the summer (stratified) and winter (mixed) seasons roughly at the inertial period $T_f \approx 18.2$ h.

The numerical results also showed that Lake Llanquihue exhibits a weak winter stratification that allows the existence of basin-scale internal motions, such as Kelvin and Poincaré waves. The theoretical periods of the wintertime Kelvin and Poincaré waves matched well energy peaks observed in the RPSD computed from the velocity field (Figure 6b,d). The Kelvin wave has a period of about 124 h, which is more than twice its summertime period. Winter basin-scale internal waves remain scarcely investigated, with the work by Rueda et al. (2003) in Lake Tahoe being one of the pioneering studies. Remarkably, the wintertime Kelvin wave observed in Lake Tahoe almost matches the Kelvin wave period identified in Lake Llanquihue. The latter suggests the existence of fundamental similarities between these two lakes, such as their Burger number. In these weakly stratified waterbodies, the effect of Earth's rotation on wind or buoyancy-driven large-scale motions can be significant. Recently, Piccolroaz et al. (2019), and Reiss et al. (2020) investigated the wind-driven, Ekman-type downwelling and upwelling during winter in Lake Garda and Lake Geneva, respectively. The authors showed that the above process supports the top-to-bottom exchange of dissolved tracers in deep, wintertime stratified basins, such as dissolved oxygen. With the pervasive strengthening of thermal stratification registered globally in lakes over the past decades and the paucity of entire winter turnover, lakes are progressively capable of hosting basin-scale internal waves that–in the past–have been mainly investigated during summertime. Future studies on the dynamics of weakly stratified water bodies will be relevant to assess deepwater ventilation in wintertime mid-latitude lakes and summertime high-latitude lakes (Priet-Mahéo et al., 2019; Ramón et al., 2020).

Our numerical results show that Lake Llanquihue hosts a large-scale gyre whose spatial structure is almost insensitive

to the change of seasons. Figures 8 and S.5 summarize the monthly circulation pattern in the upper water column. The persistence throughout the year of the large-scale cyclonic (LSC) gyre near the basin's centre is striking. The radius of the LSC gyre is approximate $R_{\mathrm{LSC}} \approx 8.8$ km and has a peripheral orbital period of about $T_{\mathrm{LSC}} \approx 750$ h. During the austral summer, the LSC gyre supports Ekman pumping and the upwelling of deep cold waters in both the pelagic and eastern lake littoral zones. LSC gyres may foster significant lateral variability and biological activity, particularly primary production. Yet, such biophysical processes are still scarcely investigated in lakes (Sepúlveda Steiner, Oscar Rodrigo, 2020; Sepúlveda Steiner et al., 2022). The growth rate of phytoplankton, or primary production, depends on various factors. However, it is boosted when sunlight and nutrients are abundantly available (MacIntyre and Jellison, 2001). Bouffard et al. (2018) showed that transient upwelling of deep cold waters during the summer season is associated with a hotspot of chlorophyll in Lake Geneva. Thus, the LSC gyre in Lake Llanquihue might likely support the upward flux of nutrients needed to fuel algae growth and the lake food chain. In situ observations of temperature, nutrients, and chlorophyll across the lake would help to test the above hypothesis.

5.3. Transport across and along the lake littoral

The increasing awareness of how lake littoral waters are becoming strongly stressed areas and collectors of their surrounding watershed processes (Jenny et al., 2020) is motivating new studies to better understand and characterize the mechanisms enhancing the exchange between nearshore and offshore regions, including wind-driven (Ulloa et al., 2018; Ramón et al., 2022) and buoyancy-driven flows (Forrest et al., 2008; Ulloa et al., 2022; Doda et al., 2022). However, little has been investigated on littoral transport in lakes. Today, hydrodynamic models allow robust numerical analysis to determine the residence time and fate of tracers in aquatic systems (see, e.g., Monsen et al., 2002; Reiss, 2021). In this study, we exploited the use of conservative passive tracers and Lagrangian tracers to investigate the physical connectivity between various sites along the coastline of Lake Llanquihue. While the study of conservative passive tracers allows estimation of how high a dissolved substance concentration can peak in a sitefar or close to the discharge zonethe Lagrangian tracers analysis helps us to identify inherent preferential pathways and time scales that connect one region to another in the lake. Cimatoribus et al. (2019) studied such preferential pathways in Lake Geneva. The authors focused on the streamlines followed by water coming from the main lake's inflow, the Rhône river. Here, we focused on characterizing the time and trajectories taken by water parcels–numerically labelled by neutral Lagrangian particles–to stream among the main urban and rural settlements along the littoral at Lake Llanquihue. Having a 3D hydrodynamic model ready to operate could help determine the fate, for instance, of contamination events that have occurred in Puerto Varas and Puerto Octay.

The circulation of Lake Llanquihue is characterised by a persistent large-scale cyclonic (LSC) gyre that occupies most of the pelagic waters. The LSC gyre interacts with shorter-lived, mesoscale anti-cyclonic (MAC) gyres localised in the grand bays of Puerto Varas and Ensenada. The LSC and MAC gyres are the determining mechanisms enabling the physical connectivity between extreme distance littoral zones. Nonetheless, the effective trajectory to stream from one site to another can be substantially larger than the Euclidean distance between two sites. The core of the LSC gyre described in 3.2 is associated with a large 'blue hole' in the autumn-winter season (see 4.2 and Figures 10-11) that attracts and keeps particles for long periods before they can escape and reach littoral waters again. The capacity of

gyres to attract and capture suspended matter has been well documented in oceanic basins (Cozar et al., 2014; Lebreton et al., 2018; Egger et al., 2020). Although mesoscale gyres have more ephemeral lives in lakes (e.g., Beletsky et al., 1999; Shimizu et al., 2007; Sepúlveda Steiner et al., 2022), they might trap and prolong the residence time of suspended matter in enclosed zones, such as bays. In particular, Lake Llanquihue is characterised by various semi-enclosed areas, including the bays of Puerto Varas, Frutillar, Puerto Octay, and Ensenada. Certainly, the impact of mesoscale gyres on the renewal of littoral waters requires further research. Future studies focusing on inner bay dynamics might provide detailed information about the processes controlling the exchange between highly stressed littoral environments and pelagic waters.

6. Concluding remarks

This paper has two main outcomes. First, it introduces the metric to quantify the 'physical connectivity' between two zones in an aquatic system. Secondly, it summarizes existing yet scattered in situ thermohydrodynamic data of Lake Llanquihue, Patagonia, Chile, and utilizes the data to develop, calibrate and validate an annual-based, three-dimensional, high-resolution numerical model to characterize the basin-scale hydrodynamics and the 'physical connectivity' among various relevant littoral areas along the lake. The study reveals that the macroscopic processes governing the spatiotemporal mass and kinetic energy distribution comprise (i) basin-scale internal gravity waves, including summer and wintertime Kelvin and Poincareé waves, (ii) inertial waves, (iii) large-scale cyclonic gyre that controls the horizontal transport over the pelagic region, and (iv) mesoscale anticyclonic gyres that emerge in the grand bays of Puerto Varas and Ensenada. The numerical results provide an overview of the annual circulation pattern reported monthly for 2016-2017. Additionally, the physical connectivity framework allows mapping the characteristic timescales and preferential pathways that the waters of Lake Llanquihue follow to stream from one littoral site to another. In particular, our results highlight the relevance played by gyres in connecting physically near and far littoral areas in a large lake, such as Llanquihue. The numerical model can be utilized to build up future studies and provide first aid information to investigate, for instance, the fate of contamination episodes in the littoral waters of Lake Llanquihue. Lastly, we stress the need for a more continuous and broader monitoring program that may underpin a sound operational numerical model for Lake Llanquihue. Such a numerical model would support the sustainable management of Lake Llanquihue and contribute to the achievement of SDGs VI, XI, and XIV, defined by the United Nations.

Acknowledgments: This research was partially supported by the supercomputing infrastructure of the National Laboratory High-Performance Computing NLHPC (ECM-02). H.N.U. acknowledges the support by the Start-up funding at the Department of Earth and Environmental Science, University of Pennsylvania. We want to thank 'Dirección General de Aguas (DGA)' and the 'Dirección de Obras Portuarias (DOP)' for providing the existing in-situ measures in Lake Llanquihue. We thank Alberto de la Fuente, Juvenal Letelier, and Xime Trujillo for their feedback on early versions of this work. Also, we thank fruitful discussions with Andrea Cimatoribus and Rafael Reiss on the performed Lagrangian and tracer numerical experiments. We also thank Rob Uittenbogaard and Leo Postma, DELFT3D-FLOW developers, for providing information on the numerical method implemented in the particle tracking module in D-Water

Quality. Last, we are grateful for the constructive feedback given by Damien Bouffard, Bernard Laval and an anonymous reviewer.

Data availability statement: The study uses the open-source numerical solver, DELFT3D-FLOW and public atmospheric data. The numerical model setting and website from where to download atmospheric data are provided in Appendix A. The Master Definition Flow (MDF) file used to set and execute DELFT3D-FLOW, as well as python scripts to download and set atmospheric forcing used to perform the numerical experiments here reported, are available through the Zenodo repository https://doi.org/10.5281/zenodo.5866250.

Appendix A. Meteorological data and numerical model setting

Meteorological data used to force the hydrodynamic model were obtained from the 'Red Agrometeorológica de Inia' and downloaded from the public website agrometeorologia.cl. We specifically used the meteorological stations surrounding Lake Llanquihue, Quilanto, Colegual, Ensenada, Rupanco, and Puerto Octay. Cloud coverage was measured at the local Airport 'El Tepual' and downloaded from the website freemeteo.cl. Data have 1 h time-averaged temporal resolution. Lake bathymetry was digitalized from the nautic chart produced by the 'Instituto Geográfico Militar' igm.cl.

We run DELFT-FLOW using a Cartesian mesh of 314×308 grid points in the North-South and East-West axis, respectively, that set a grid size of $\Delta x = \Delta z = 130$ m. In the vertical axis, we used 20 layers, spatially distributed at resolving vertical gradients in the upper water column. The RANS equations of motion for the momentum, heat, and tracer transport were integrated over time using a time-step of $\Delta t = 1$ min. The momentum equation considered a space-varying Coriolis frequency whose reference value corresponds to the South latitude -41.33°. The lake's surface was subjected to wind and heat fluxes. For this deep lake, we set the bottom boundary to be shear-free and adiabatic. Physical parameters used include the gravity acceleration $g = 9.81\ \mathrm{m\,s^{-2}}$, the water and air reference densities, $\rho_0 = 1000\ \mathrm{kg\,m^{-3}}$ and $\rho_a = 1\ \mathrm{kg\,m^{-3}}$, respectively, and a zero constant salinity. The wind drag coefficient was set to be wind speed-dependent, following the empirical fitting curves shown in Wüest and Lorke (2003) (see Delft-FLOW manual). Bottom roughness and dissipation were controlled by a calibrated Chezy coefficient, $C_r \approx 150\ \mathrm{m^{1/2}\,s^{-1}}$ (A.1) shown in Figure A.1. This coefficient allows maximizing the model skill metric (1) for the numerically resolved velocity field (4).

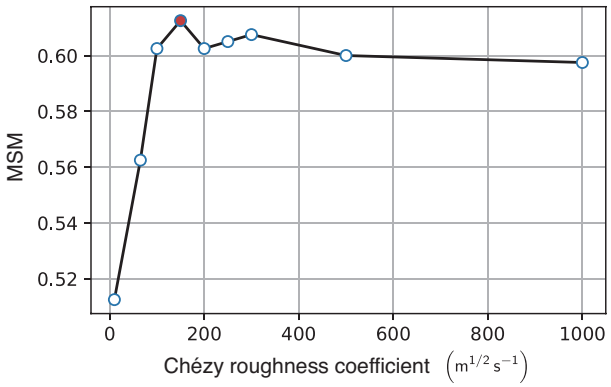

Figure A.1: Model skill metric (MSM) as a function of the Chézy roughness coefficient, C_r. The MSM is maximized at about $C_r \approx 150$.

Following the technical report by Gerritsen et al. (2008) and the validation of DELFT3D in Lake Grevelingen, the background horizontal turbulent viscosity and diffusivity were set to be $\nu^{(\mathrm{h})}_{\mathrm{back}} = \kappa^{(\mathrm{h})}_{\mathrm{back}} = 0.5\ \mathrm{m}^2\,\mathrm{s}^{-1}$, whereas the background vertical turbulent viscosity and diffusivity were set to be $\nu^{(\mathrm{v})}_{\mathrm{back}} = \kappa^{(\mathrm{v})}_{\mathrm{back}} = 5 \times 10^{-6}\ \mathrm{m}^2\,\mathrm{s}^{-1}$. The fluid density was determined from the state variables (temperature and salinity) via the UNESCO equation of state, built-in Delft3D. We used the 'ocean module' in DELFT3D for computing the heat budget in the lake. The input parameters to compute the heat fluxes in the total heat balance equation include the sky cloud coverage (in %), relative humidity, the air temperature, and surface water temperature, wind, incoming solar radiation, and adopting a Secchi disc of 21 m, a Dalton number for the evaporative heat flux of (1.50×10^{-3}), and a Stanton number for heat convection of 1.45×10^{-3}. For more information, we refer the reader to section 9.8 of Delft-FLOW manual. Thus, space varying heat fluxes were estimated using the 1 h resolution meteorological data, which then were linearly interpolated at the model integration time resolution, i.e., $\Delta t = 1$ min. The model was initialized on August 1st, 2015, at rest $\bar{v} = 0$ and uniform temperature $T = 10.5°\mathrm{C}$. We used the 'Cyclic method' for the advection schemes for the momentum and heat transport equations based on the ADI-method (Stelling and Leendertse, 1992). The Cyclic method is built on implicit time integration of both advection and diffusion, and it uses a Forester filter to remove non-physical spurious oscillations (Forester, 1977).

The numerical simulations were run in the National Laboratory of High-Performance Computing (NLHPC), Chile. The post-processing and numerical analyses of the 3D velocity, temperature and tracers fields reported in this paper are based on a 1 h model output resolution.

Appendix B. Observation-Model comparison

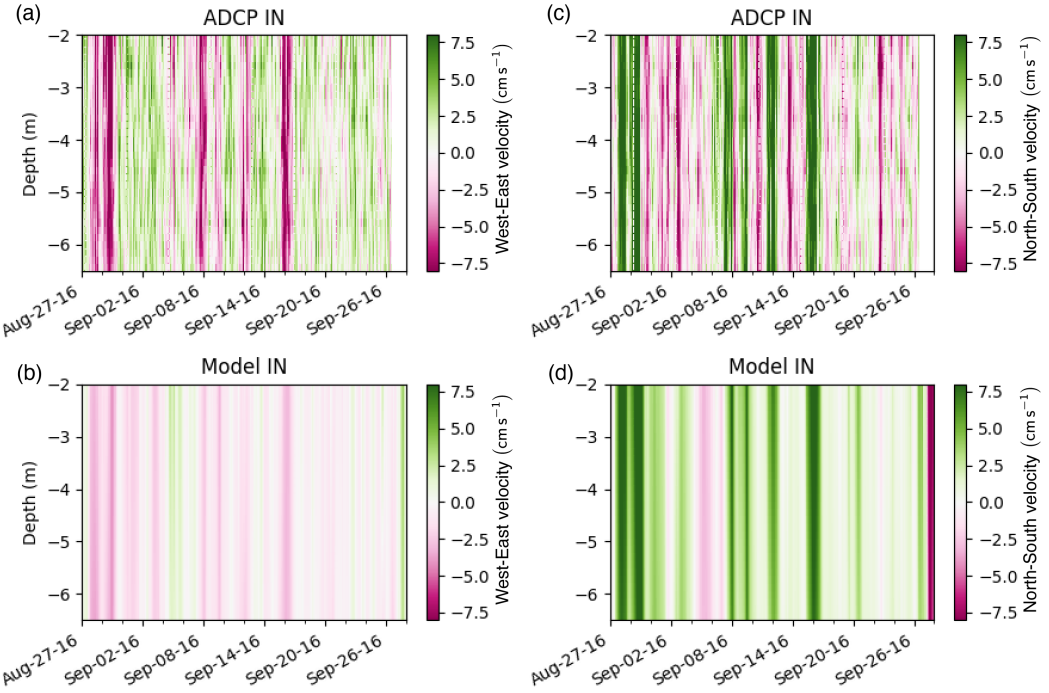

Figure B.1: Comparison between ADCP observations and numerical model at IN location shown in Figure 2(e), during late summer/early spring 2016. Left panels (a) and (b) compare the ADCP West-East velocity profile as a function of time with the model results at the closest grid point. Right panels compare ADCP North-South velocity profiles as a function of time with the model results at the closest grid-point.

Figure B.1 shows a one-to-one model-observation comparison for the velocity components in the winter period of 2016. The ADCP and the model signals show coherent phases over time, yet we observe the model underestimates the West-East (almost cross-shore) velocity component measured by the ADCP (Figure B.1a,c). Although the latter mismatch is undesirable, it is not entirely surprising since the ADCP was deployed near the shore, where the model cannot fully resolve topographically-controlled processes that affect the cross-shore velocity component. In contrast, the South-North (almost along-the-shore) velocity component of our numerical model reproduces well both the magnitude and phase of the field observations (Figure B.1b,d). Indeed, the latter velocity component should be less sensitive to the topography; therefore, the better match between the model and the observations confirms the robustness achieved by the numerical model.

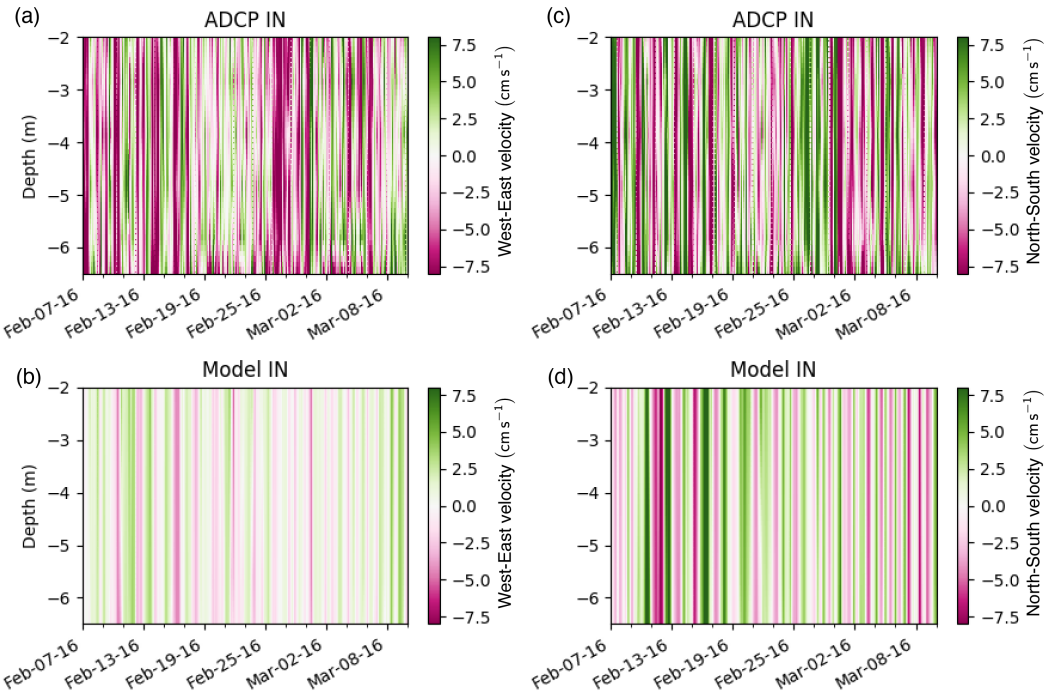

Figure B.2: Comparison of ADCP observations and numerical model at IN location shown in Figure 2(e), during mid-summer 2016. Left panels (a) and (b) compare the ADCP West-East velocity profile as a function of time with the model results at the closest grid point. Right panels compare ADCP North-South velocity profiles as a function of time with the model results at the closest grid-point.

Figure B.2 shows the one-to-one comparison between the numerical model and the ADCP during the summer period of 2016. During this period, the numerical model exhibits a lower performance. Like in the winter period, the model underestimates the West-East velocity component magnitude (Figure B.2a,c) while capturing well the magnitude of the South-East velocity component (Figure B.2b,d). The phase coherence is less coherent, and in the summer, the ADCP signal has high frequencies that the model does not capture. We stress that detailed process-based nearshore studies require to resolve the nearshore topographic features correctly.

Figure B.3 shows the wavelet spectral signature of both the ADCP measurements and the model results for summer and winter seasons in the nearshore of Iansa Norte (Figure 2e). We observed that the model does not capture the energy in periods shorter than 10 h, yet it well reproduces periods above 20 h in the summer season (Figure B.3a,b). In the winter season, most of the energy is contained at frequencies associated with periods longer than 40 h, which the model captures. The above results set the scopes for the numerical approach and support the use of our model to study low frequency processes associated with large- and basin-scale motions in Lake Llanquihue.

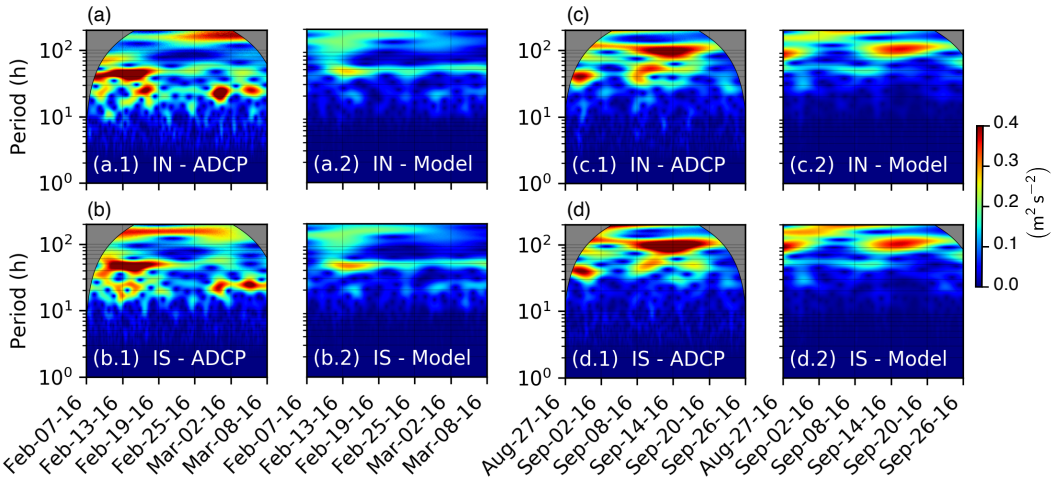

Figure B.3: Comparison between observations and numerical model at IN and IS locations shown in Figure 1. Cyclonic wavelet spectra at 5.5 m depth.

References

Almanza, V., Pedreros, P., Laughinghouse, H. D., Félez, J., Parra, O., Azócar, M., and Urrutia, R. (2019). Association between trophic state, watershed use, and blooms of cyanobacteria in south-central Chile. *Limnologica*, 75:30–41.

Amadori, M., Piccolroaz, S., Dijkstra, H. A., and Toffolon, M. (2020). What makes an elongated lake 'large'? scales from wind-driven steady circulation on a rotating earth. *J. Great Lakes Res.*, 46(4):703–717.

Antenucci, J. P. and Imberger, J. (2001). Energetics of long internal gravity waves in large lakes. *Limnol. Oceanogr.*, 46(7):1760–1773.

Ballesteros, T. A. (2019). Assessment of visual landscape in Llanquihue lake shore, Región de los Lagos, Chile. Master thesis, Universidad Católica de Temuco.

Baracchini, T., Wüest, A., and Bouffard, D. (2020). Meteolakes: An operational online three-dimensional forecasting platform for lake hydrodynamics. *Water Res.*, 172:115529.

Beletsky, D., Saylor, J. H., and Schwab, D. J. (1999). Mean circulation in the Great Lakes. *J. Great Lakes Res.*, 25(1):78–93.

Biemond, B., Amadori, M., Toffolon, M., Piccolroaz, S., Haren, H. V., and Dijkstra, H. A. (2021). Deep-mixing and deep-cooling events in Lake Garda: Simulation and mechanisms. *J. Limnol.*, 80(2).

Bouffard, D., Boegman, L., and Rao, Y. R. (2012). Poincaré wave-induced mixing in a large lake. *Limnol. Oceanogr.*, 57(4):1201–1216.

Bouffard, D., Kiefer, I., Wüest, A., Wunderle, S., and Odermatt, D. (2018). Are surface temperature and chlorophyll in a large deep lake related? An analysis based on satellite observations in synergy with hydrodynamic modelling and in-situ data. *Remote Sens. Environ.*, 209:510–523.

Bouffard, D. and Lemmin, U. (2013). Kelvin waves in Lake Geneva. *J. Great Lakes Res.*, 39(4):637–645.

Bouffard, D. and Wüest, A. (2019). Convection in lakes. *Annu. Rev. Fluid Mech.*, 51(1):189–215.

Campos, H. (1984). Limnological study of Araucanian lakes (Chile). *SIL Proceedings, 1922-2010*, 22(2):1319–1327.

Campos, H., Steffens, W., Agüero, G., Parra, O., and Zuñiga, L. (1988). Limnological study of Lake Llanquihue (Chile). Morphometry, physics, chemistry, plankton and primary productivity. *Arch. Hydrobiol.*, 81(1):37–67.

Choi, J., Troy, C. D., Hsieh, T.-C., Hawley, N., and McCormick, M. J. (2012). A year of internal Poincaré waves in southern Lake Michigan. *J. Geophys. Res.: Oceans*, 117(C7):n/a–n/a.

Cimatoribus, A. A., Lemmin, U., and Barry, D. A. (2019). Tracking Lagrangian transport in Lake Geneva: A 3D numerical modeling investigation. *Limnol. Oceanogr.*, 64(3):1252–1269.

Cozar, A., Echevarria, F., Gonzalez-Gordillo, J. I., Irigoien, X., Ubeda, B., Hernandez-Leon, S., Palma, A. T., Navarro, S., de Lomas, J. G., Ruiz, A., de Puelles, M. L. F., and Duarte, C. M. (2014). Plastic debris in the open ocean. *Proc. Natl. Acad. Sci.*, 111(28):10239–10244.

Csanady, G. T. (1975). Hydrodynamics of large lakes. *Annu. Rev. Fluid Mech.*, 7(1):357–386.

de la Fuente, A., Shimizu, K., Imberger, J., and Niño, Y. (2008). The evolution of internal waves in a rotating, stratified, circular basin and the influence of weakly nonlinear and nonhydrostatic accelerations. *Limnol. Oceanogr.*, 53(6):2738–2748.

de la Fuente, A., Shimizu, K., Niño, Y., and Imberger, J. (2010). Nonlinear and weakly nonhydrostatic inviscid evolution of internal gravitational basin-scale waves in a large, deep lake: Lake Constance. *J. Geophys. Res.*, 115(C12).

De los Ríos, P. and Soto, D. (2007). Eutrophication and dominance of Daphnids (crustacea) in a deep patagonian lake (Lake Llanquihue, Chile). *Polish Journal of Ecology*, 51(1):191–193.

Deltares (2014). Delft3d-flow user manual, version:3.15.34158. Technical report, Deltares.

Doda, T., Ramón, C. L., Ulloa, H. N., and Bouffard, D. (2022). Seasonal variability of density currents induced by differential cooling. *Hydrol. Earth Syst. Sci*.

Donoso, G., editor (2018). *Water Policy in Chile*. Springer International Publishing.

Dorostkar, A., Boegman, L., and Pollard, A. (2017). Three-dimensional simulation of high-frequency nonlinear internal wave dynamics in Cayuga Lake. *J. Geophys. Res. Oceans*, 122(3):2183–2204.

Egger, M., Sulu-Gambari, F., and Lebreton, L. (2020). First evidence of plastic fallout from the North Pacific garbage patch. *Sci. Rep.*, 10(1).

Fernández Castro, B., Bouffard, D., Troy, C., Ulloa, H. N., Piccolroaz, S., Sepúlveda Steiner, O., Chmiel, H. E., Serra Moncadas, L., Lavanchy, S., and Wüest, A. (2021). Seasonality modulates wind-driven mixing pathways in a large lake. *Communications Earth & Environment*, 2(1).

Forester, C. (1977). Higher order monotonic convective difference schemes. *J. Comput. Phys.*, 23(1):1–22.

Forrest, A. L., Laval, B. E., Pieters, R., and Lim, D. S. S. (2008). Convectively driven transport in temperate lakes. *Limnol Oceanogr*, 53(5part2):2321–2332.

García, P. E., Queimaliños, C., and Diéguez, M. C. (2019). Natural levels and photo-production rates of hydrogen peroxide (h2o2) in Andean Patagonian aquatic systems: Influence of the dissolved organic matter pool. *Chemosphere*, 217:550–557.

Geller, W. (1992). The temperature stratification and related characteristics of Chilean lakes in midsummer. *Aquat. Sci.*, 54(1):37–57.

Gerritsen, H., de Goede, E. D., Platzek, F. W., van Kester, J., Genseberger, M., and Uittenbogaard, R. (2008). Validation Document Delft3D-FLOW: A software system for 3d flow simulations. Technical Report X0365, M3470, Deltares.

Gómez-Giraldo, A., Imberger, J., and Antenucci, J. P. (2006). Spatial structure of the dominant basin-scale internal waves in Lake Kinneret. *Limnol. Oceanogr.*, 51(1):229–246.

Herdendorf, C. E. (1982). Large Lakes of the World. *J. Great Lakes Res.*, 8(3):379–412.

Iriarte, J. L. (2018). Natural and human influences on marine processes in Patagonian subantarctic coastal waters. *Front. Mar. Sci.*, 5.

Jenny, J.-P., Anneville, O., Arnaud, F., Baulaz, Y., Bouffard, D., Domaizon, I., Bocaniov, S. A., Chèvre, N., Dittrich, M., Dorioz, J.-M., Dunlop, E. S., Dur, G., Guillard, J., Guinaldo, T., Jacquet, S., Jamoneau, A., Jawed, Z., Jeppesen, E., Krantzberg, G., Lenters, J., Leoni, B., Meybeck, M., Nava, V., Nõges, T., Nõges, P., Patelli, M., Pebbles, V., Perga, M.-E., Rasconi, S., Ruetz, C. R., Rudstam, L., Salmaso, N., Sapna, S., Straile, D., Tammeorg, O., Twiss, M. R., Uzarski, D. G., Ventelä, A.-M., Vincent, W. F., Wilhelm, S. W., Wängberg, S.-Å., and Weyhenmeyer, G. A. (2020). Scientists' warning to humanity: Rapid degradation of the world's large lakes. *J. Great Lakes Res.*, 46(4):686–702.

Large, W. G. and Pond, S. (1981). Open ocean momentum flux measurements in moderate to strong winds. *J. Phys. Oceanogr.*, 11(3):324–336.

Launder, B. and Spalding, D. (1974). The numerical computation of turbulent flows. *Comput. Methods Appl. Mech. Eng.*, 3(2):269–289.

Laval, B., Imberger, J., Hodges, B. R., and Stocker, R. (2003). Modeling circulation in lakes: Spatial and temporal variations. *Limnol. Oceanogr.*, 48(3):983–994.

Lebreton, L., Slat, B., Ferrari, F., Sainte-Rose, B., Aitken, J., Marthouse, R., Hajbane, S., Cunsolo, S., Schwarz, A., Levivier, A., Noble, K., Debeljak, P., Maral, H., Schoeneich-Argent, R., Brambini, R., and Reisser, J. (2018). Evidence that the great Pacific garbage patch is rapidly accumulating plastic. *Sci. Rep.*, 8(1).

Lin, S., Boegman, L., Valipour, R., Bouffard, D., Ackerman, J., and Zhao, Y. (2021). Three-dimensional modeling of sediment resuspension in a large shallow lake. *J. Great Lakes Res.*

Lorke, A., Peeters, F., and Bäuerle, E. (2006). High-frequency internal waves in the littoral zone of a large lake. *Limnol. Oceanogr.*, 51(4):1935–1939.

MacIntyre, S. and Jellison, R. (2001). Nutrient fluxes from upwelling and enhanced turbulence at the top of the pycnocline in Mono Lake, California. *Hydrobiologia*, 466(1/3):13–29.

Monsen, N. E., Cloern, J. E., Lucas, L. V., and Monismith, S. G. (2002). A comment on the use of flushing time, residence time, and age as transport time scales. *Limnol. Oceanogr.*, 47(5):1545–1553.

Mouginot, J. and Rignot, E. (2015). Ice motion of the Patagonian icefields of South America: 1984–2014. *Geophys. Res. Lett.*, 42(5):1441–1449.

Piccolroaz, S., Amadori, M., Toffolon, M., and Dijkstra, H. A. (2019). Importance of planetary rotation for ventilation processes in deep elongated lakes: Evidence from Lake Garda (Italy). *Sci. Rep.*, 9(1).

Porter, S. C. (1981). Pleistocene glaciation in the Southern Lake District of Chile. *Quat. Res.*, 16(3):263–292.

Postma, L., van Beek, J. K. L., van den Boogaard, H. F. P., and Stelling, G. S. (2012). Consistent and efficient particle tracking on curvilinear grids for environmental problems. *Internat. J. Numer. Methods Fluids*, 71(10):1226–1237.

Preusse, M., Freistühler, H., and Peeters, F. (2012). Seasonal variation of solitary wave properties in Lake Constance. *J. Geophys. Res. Oceans*, 117(C4):n/a–n/a.

Priet-Mahéo, M. C., Ramón, C. L., Rueda, F. J., and Andradóttir, H. Ó. (2019). Mixing and internal dynamics of a medium-size and deep lake near the Arctic Circle. *Limnol. Oceanogr.*, 64(1):61–80.

Ramón, C. L., Priet-Mahéo, M. C., Rueda, F. J., and Andradóttir, H. (2020). Inflow dynamics in weakly stratified lakes subject to large isopycnal displacements. *Water Resour. Res.*, 56(8).

Ramón, C. L., Ulloa, H. N., Doda, T., and Bouffard, D. (2022). Flushing the lake littoral region: The interaction of differential cooling and mild winds. *Water Resour. Res.*, 58(3).

Reiss, R. S. (2021). *Dynamics of wind-induced coastal upwelling and interbasin exchange in Lake Geneva during winter: Implications for deepwater renewal*. PhD thesis, École Polytechnique Fédérale de Lausanne.

Reiss, R. S., Lemmin, U., Cimatoribus, A. A., and Barry, D. A. (2020). Wintertime coastal upwelling in Lake Geneva: An efficient transport process for deepwater renewal in a large, deep lake. *J. Geophys. Res. Oceans*, 125(8).

Rey, A., Mulligan, R., Ferreira da Silva, A. M., Filion, Y., Champagne, P., and Boegman, L. (2021). Three-dimensional hydrodynamic behavior of an operational waste-stabilization pond. *J. Environ. Eng.*, 147(2):05020009.

Rozas, C., de la Fuente, A., Ulloa, H., Davies, P., and Niño, Y. (2014). Quantifying the effect of wind on internal wave resonance in Lake Villarrica, Chile. *Environ. Fluid Mech.*, 14 (4):849–871.

Rueda, F. J., Schladow, G., and Pálmarsson, S. Ó. (2003). Basin-scale internal wave dynamics during a winter cooling period in a large lake. *J. Geophys. Res.*, 108(C3).

Sakai, T. and Redekopp, L. G. (2010). A weakly nonlinear evolution model for long internal waves in a large lake. *J. Fluid Mech.*, 656:260–297.

Sepúlveda Steiner, O., Forrest, A. L., Mcinerney, J., Fernández Castro, B., Lavanchy, S., Wüest, A., and Bouffard, D. (2022). Spatial variability of turbulent mixing from an underwater glider in a large, deep stratified lake. *Earth and Space Science Open Archive*, page 31.

Sepúlveda Steiner, Oscar Rodrigo (2020). *Mixing processes and their ecological implications: From vertical to lateral variability in stratified lakes*. PhD thesis, EPFL, Switzerland.

Shimizu, K., Imberger, J., and Kumagai, M. (2007). Horizontal structure and excitation of primary motions in a strongly stratified lake. *Limnol Oceanogr*, 52(6):2641–2655.

Soto, D. and Campos, H. (1995). *Los lagos oligrotróficos asociados al bosque templado del sur de Chile*. Ed. Universitaria. 317-334.

Stelling, G. S. and Leendertse, J. J. (1992). Approximation of convective processes by cyclic aoi methods. In *Estuarine and coastal modeling, Proceedings 2nd Conference on Estuarine and Coastal Modeling, ASCE, Tampa*, pages 771–782.

Ulloa, H. N., Davis, K. A., Monismith, S. G., and Pawlak, G. (2018). Temporal variability in thermally driven cross-shore exchange: The role of semidiurnal tides. *J. Phys. Oceanogr.*, 48(7):1513–1531.

Ulloa, H. N., de la Fuente, A., and Niño, Y. (2014). An experimental study of the free evolution of rotating, nonlinear internal gravity waves in a two-layer stratified fluid. *J. Fluid Mech.*, 742:308–339.

Ulloa, H. N., Ramón, C. L., Doda, T., Wüest, A., and Bouffard, D. (2022). Development of overturning circulation in sloping waterbodies due to surface cooling. *J. Fluid Mech.*, 930.

Ulloa, H. N., Winters, K., de la Fuente, A., and Niño, Y. (2015). Degeneration of internal Kelvin waves in a continuous two-layer stratification. *J. Fluid Mech.*, 777:68–96.

Valerio, G., Pilotti, M., Marti, C. L., and Imberger, J. (2012). The structure of basin-scale internal waves in a stratified lake in response to lake bathymetry and wind spatial and temporal distribution: Lake Iseo, Italy. *Limnol. Oceanogr.*, 57(3):772–786.

Valipour, R., Boegman, L., Bouffard, D., and Rao, Y. R. (2017). Sediment resuspension mechanisms and their contributions to high-turbidity events in a large lake. *Limnol. Oceanogr.*, 62(3):1045–1065.

Weatherill, N. (1992). Delaunay triangulation in computational fluid dynamics. *Computers & Mathematics with Applications*, 24(5-6):129–150.

Willis, M. J., Melkonian, A. K., Pritchard, M. E., and Rivera, A. (2012). Ice loss from the Southern Patagonian ice field, South America, between 2000 and 2012. *Geophys. Res. Lett.*, 39(17):n/a–n/a.

Willmott, C. J. (1981). On the validation of models. *Phys. Geogr.*, 2:184–194.

Winters, K. B., Lombard, P. N., Riley, J. J., and D'Asaro, E. A. (1995). Available potential energy and mixing in density-stratified fluids. *J. Fluid Mech.*, 289:115–128.

Woelfl, S., Nimptsch, J., Oyarzun, C. E., Caputo, L., Bertran, C., Grandjean, M., Jaramillo, J., Schories, D., and Steffen, W. (2013). Evaluación del estado ambiental de los lagos utilizandos para actividades de acuicultura en la zona sur austral de Chile. Report 4728-42-LP12, Universidad Austral de Chile.

Wüest, A. and Lorke, A. (2003). Small-Scale Hydrodynamics in Lakes. *Annu. Rev. Fluid Mech.*, 35(1):373–412.

Supplementary Material A. "Basin-scale hydrodynamics and physical connectivity in a Great Patagonian Lake" by Javiera Abarca, Hugo N. Ulloa & Yarko Niño.

The supplementary materials for this article comprises 13 figures (S.1-S.13).

Figure S.1: Wind field 10 meters above the lake surface reconstructed from linearly interpolating in-situ wind data from six meteorological stations near the lake for Oct-21-2016, 12:00-13:00 h. Red arrows show the one-hour average wind direction and magnitude at each meteorological station site. The red arrow on the lake's center was obtained from the WRF model (Weather Research and Forecasting), developed by the Geophysics Department at Universidad de Chile http://walker.dgf.uchile.cl/Explorador/Eolico2/.

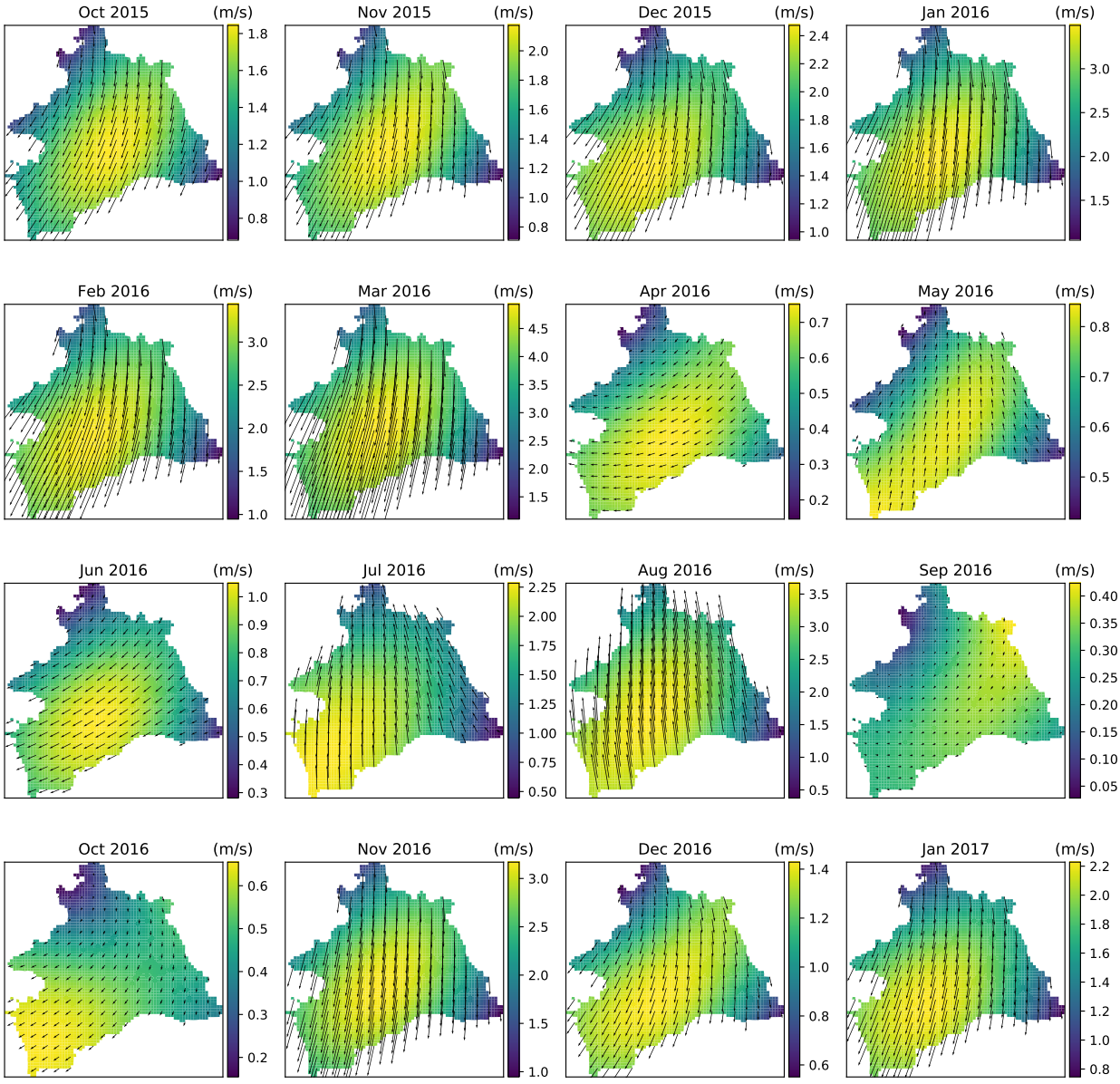

Figure S.2: Monthly mean wind pattern at 10 m above the lake's surface.

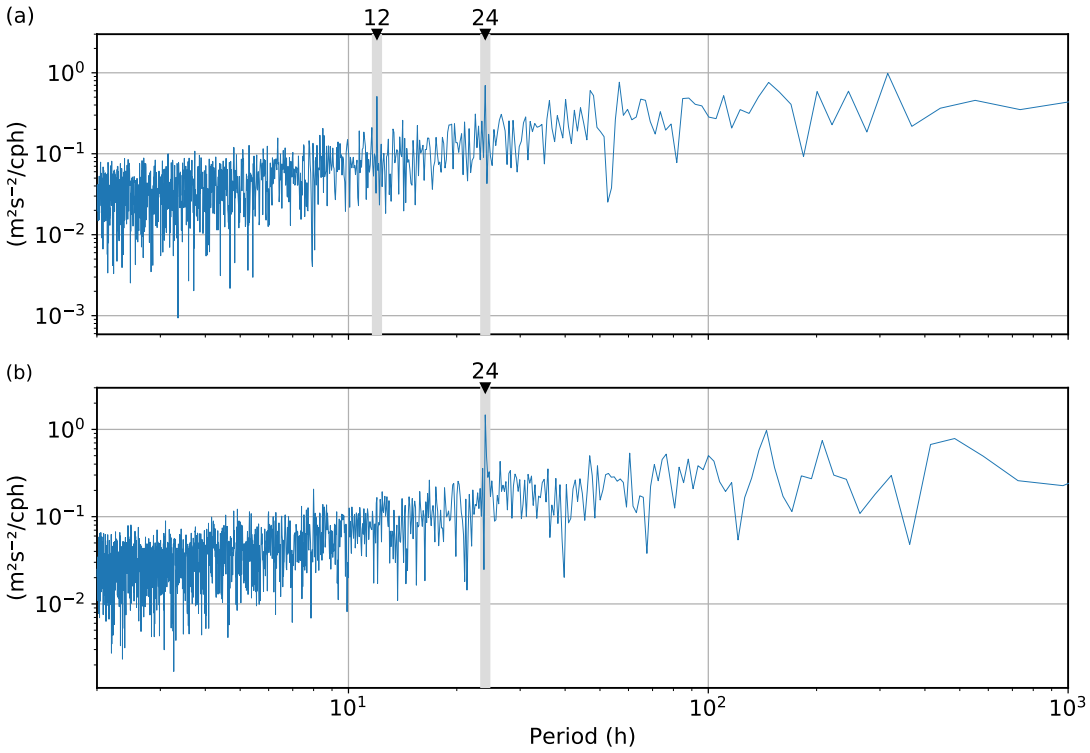

Figure S.3: Power spectral density (PSD) of wind magnitude during (a) May-Aug (2016) and (b) December (2016)-March (2017) periods. Black triangles on top of each PSD indicate the energy peak periods in hours.

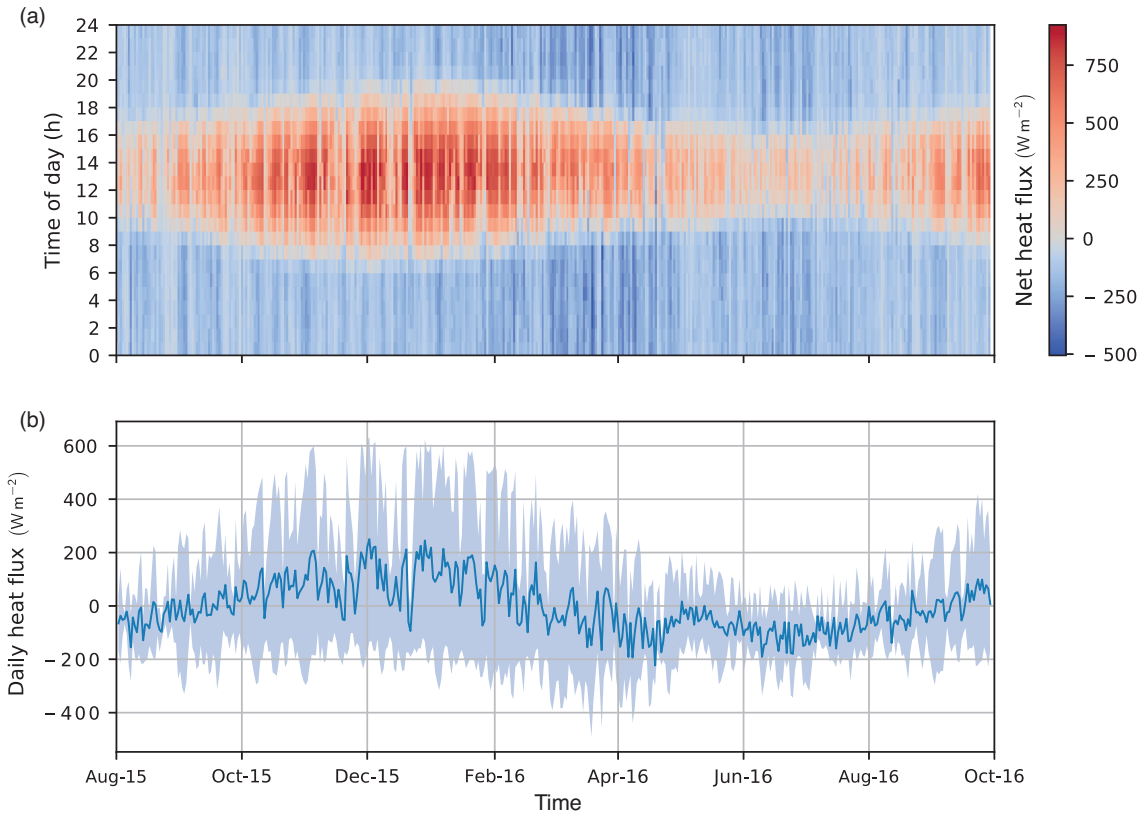

Figure S.4: Panel (a) shows spatially averaged net surface heat flux $\langle H_{\mathrm{n}} \rangle_{\mathrm{s}}$ in Lake Llanquihue from August 2015 to October 2016. The vertical and horizontal axes show the daily and annual evolution of $\langle H_{\mathrm{n}} \rangle_{\mathrm{s}}$, respectively. Panel (b) shows the spatially and day averaged net surface heat flux, $\langle H_{\mathrm{n}} \rangle_{\mathrm{s,d}}$ (vertical axis), as a function of time (horizontal axis) along with its daily-based standard deviation (shaded area). A positive value of H_{n} means a gain of heat in the lake, while a negative value means a loss of heat from the lake.

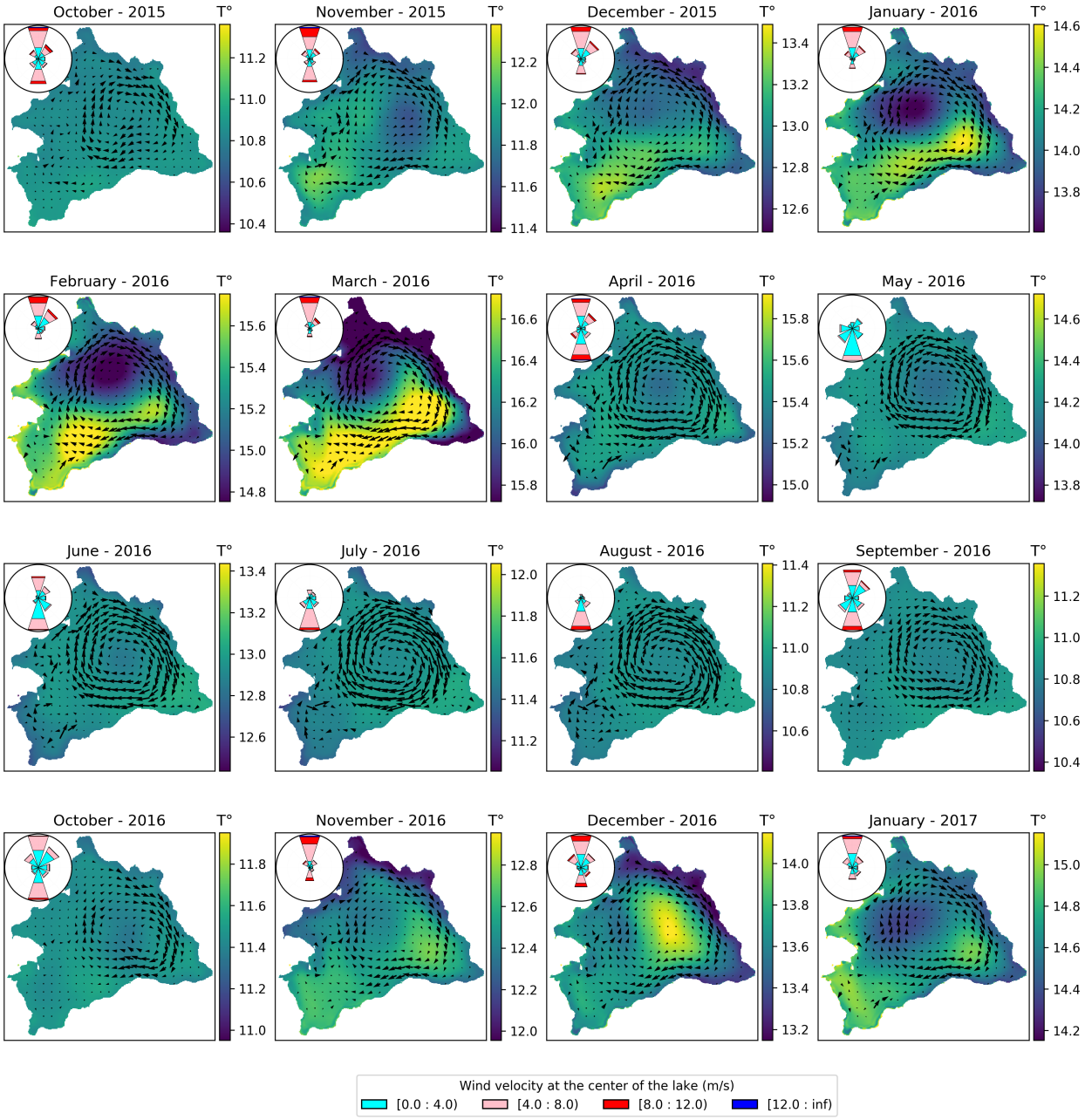

Figure S.5: Monthly mean circulation pattern between 62 and 79 m depth, superimposed on water temperature at 37 m depth. Each panel shows the wind rose for the interpolated wind at the lake center.

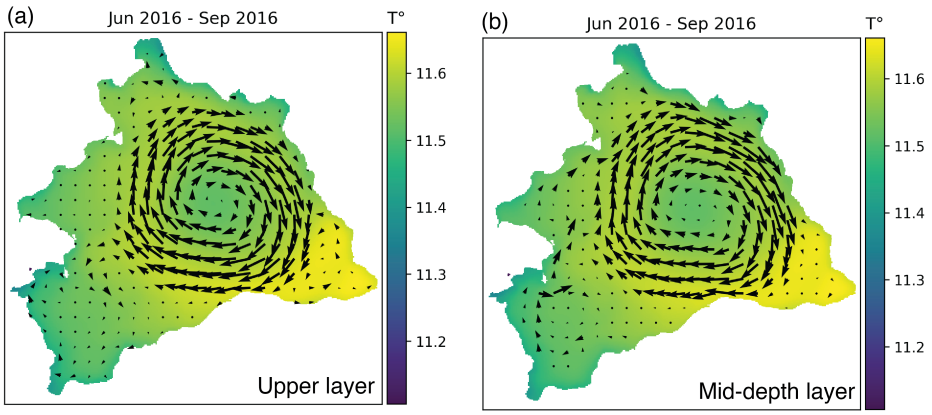

Figure S.6: (a) Mean circulation pattern between 4 and 36 m depth from June to September 2016. (b) Mean circulation pattern between 62 and 79 m depth from June to September 2016. Colormap shows the water temperature at 37 m depth.

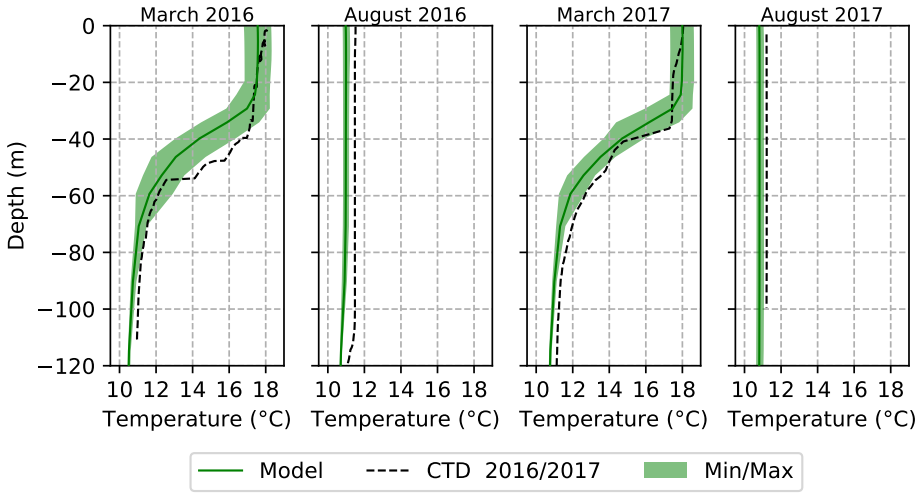

Figure S.7: Bi-annual CTD casts sampled by Dirección General de Aguas (DGA) along with numerical results for the sampling site for 2016 and 2017.

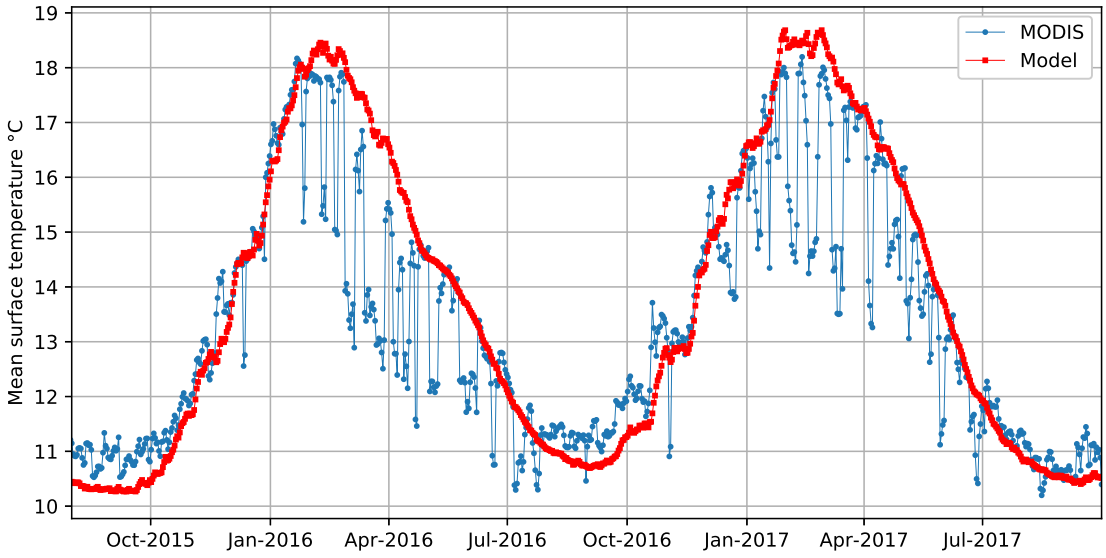

Figure S.8: Time series of means surface temperature derived from MODIS images and the numerical model.

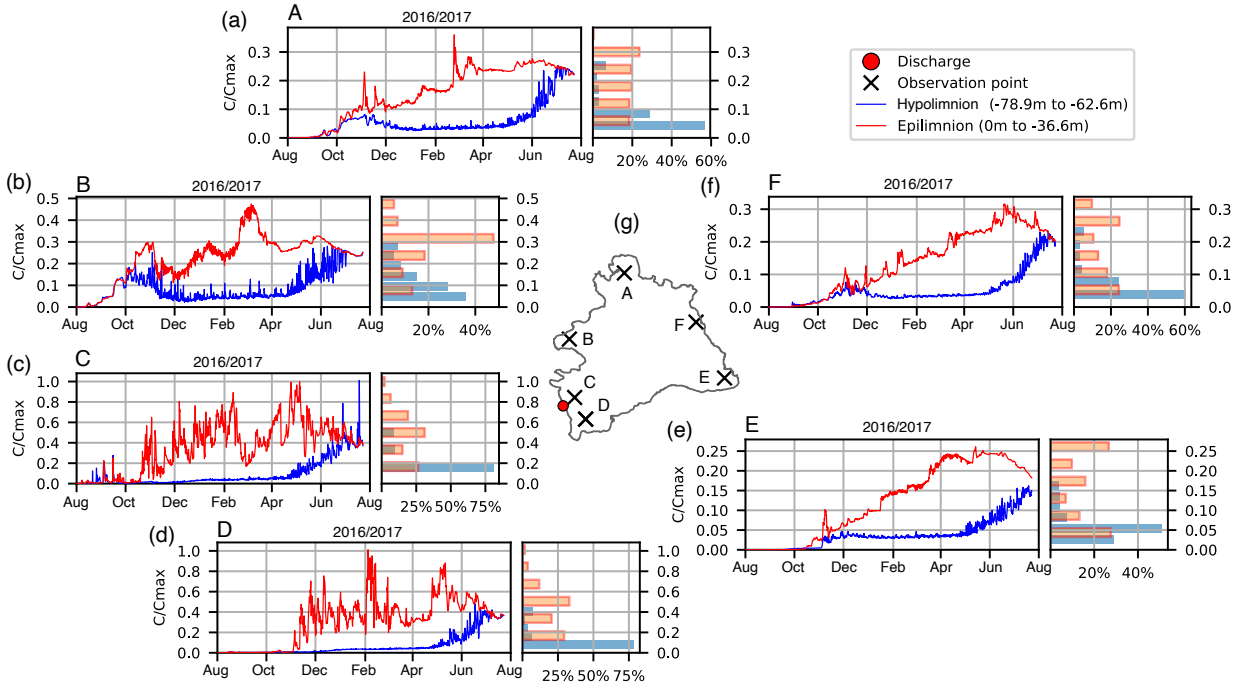

Figure S.9: Numerical model results: Tracer experiment for 08/2016-08/2017. Crosses denote numerical monitoring points for the tracer released from the shores of Llanquihue city (red circle). Panels show time series of the normalized tracer concentration $c/c_{\max}$ at each location. Red lines denote $c/c_{\max}$ within the surface waters, 0-36.6 m, whereas blue lines denote $c/c_{\max}$ for deep waters, 62.6-78.9 m. Notice that the scale for $c/c_{\max}$ may change from panel to panel.

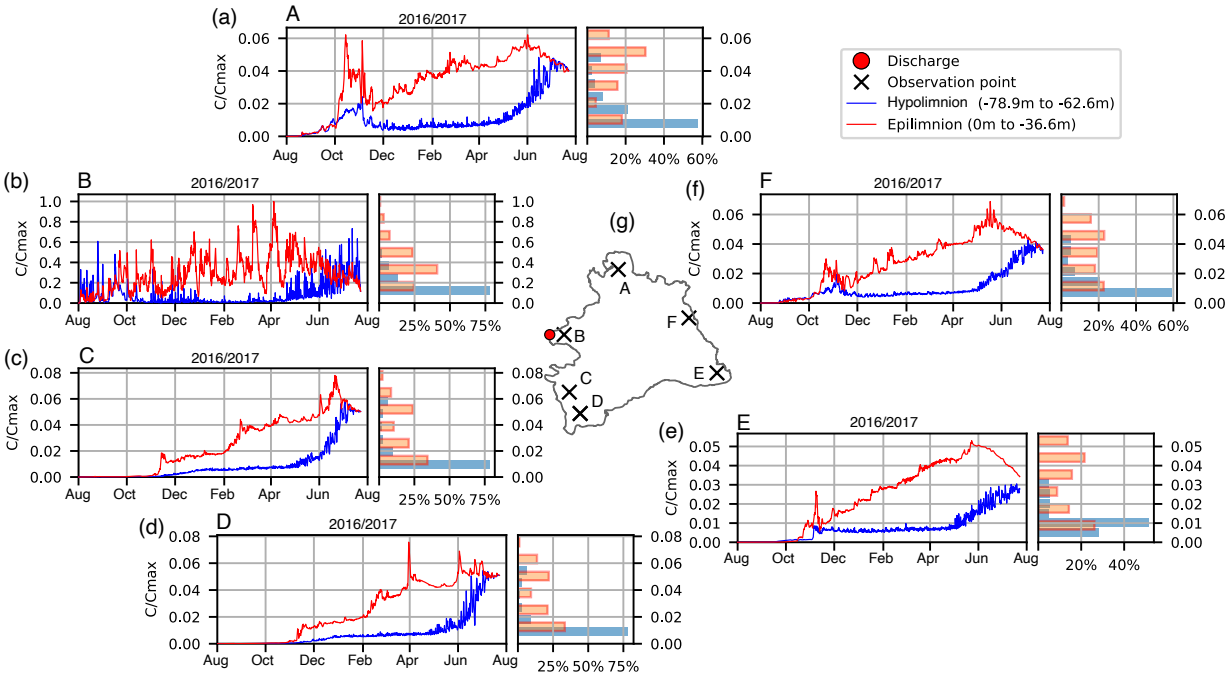

Figure S.10: Numerical model results: Tracer experiment for 08/2016-08/2017. Crosses denote numerical monitoring sites for the tracer released from the shores of Frutillar city (red circle). Panels show the time series of the normalized tracer concentration $c/c_{\max}$ at each location. Red lines denote $c/c_{\max}$ within the surface waters, 0-36.6 m, whereas blue lines denote $c/c_{\max}$ for deep waters, 62.6-78.9 m. Notice that the scale for $c/c_{\max}$ may change from panel to panel.

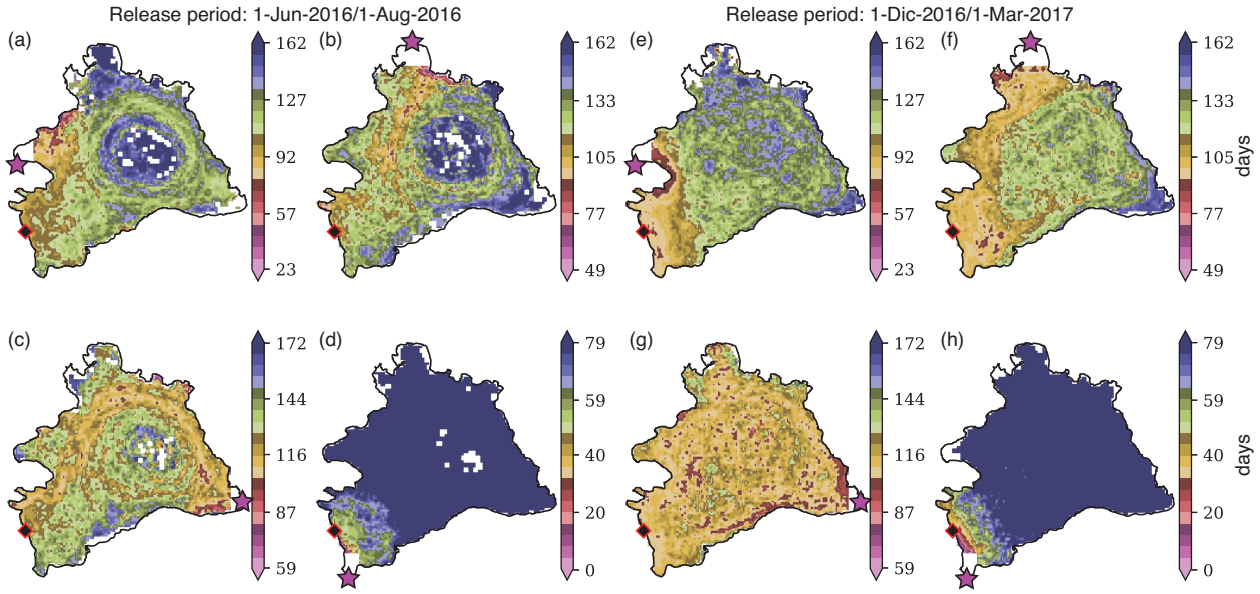

Figure S.11: Lagrangian tracer analysis: maps of the mean residence time and preferential pathways throughout Lake Llanquihue. Left panels show results from the autumn-winter (AW) season (Jun-1-2016/Aug-1-2016), whereas right panels show results from the spring-summer (SS) season (Dec-1-2016/Mar-1-2017). The colorbar denotes times taken by Lagrangian tracers released from Llanquihue to reach the nearshore region of (a,e) Frutillar city, (b,f) Puerto Octay town, (c,g) Ensenada town, and (d,h) Puerto Varas city.

Figure S.11 characterizes the time taken by particles to flow from Llanquihue to Frutillar (panels a and e), Puerto Octay (panels b and f), Ensenada (panels c and g), and Puerto Varas (panels d and h). Particles get in Frutillar following the western shoreline in AW and SS periods, whereas to get in Puerto Octay, the particles follow similar pathways as those taken from Puerto Varas. The preferential pathway to reach Ensenada is, in both seasons, through the cyclonic trajectory set by the LSC gyre. This latter pathway is particularly distinctive in the AW season (Figure S.11c). Reaching Puerto Varas from Llanquihue, particles also follow a pathway almost parallel to the shoreline. However, the trajectory distribution is not quite the same as that in the opposite direction (Llanquihue from Puerto Varas), as we can observe by comparing Figures S.11(d,h) with Figures 10(a,e). It is therefore relevant to highlight that the metrics associated with the physical connectivity between two neighboring regions in a lake depend on the relative position of such regions with respect to the preferential direction of the local circulation.

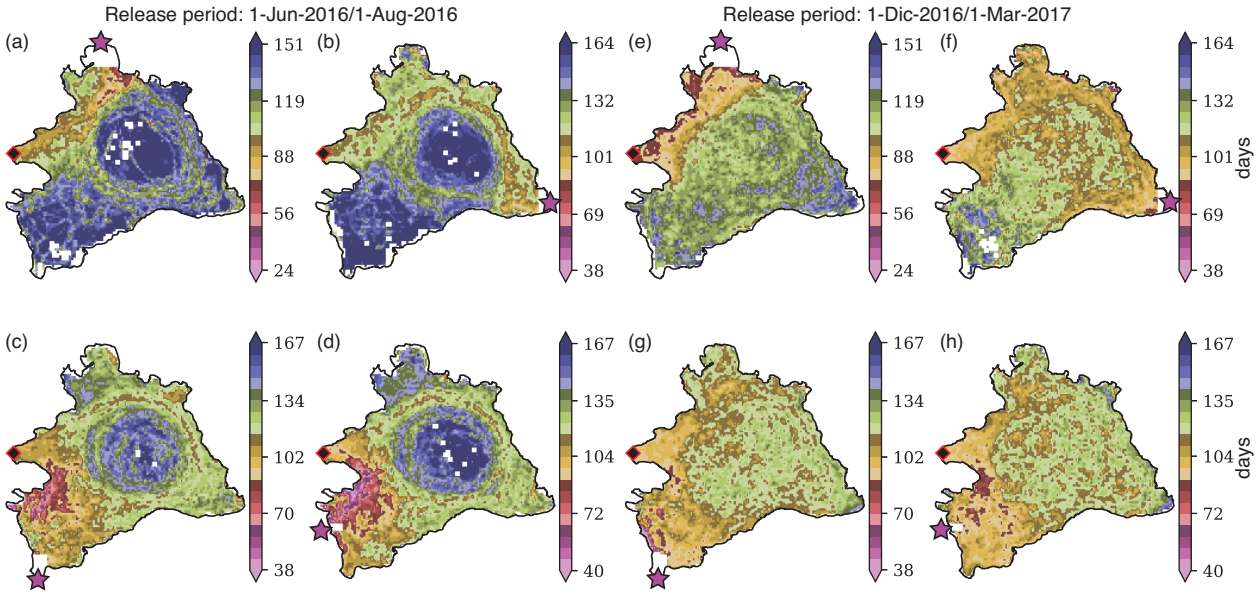

Figure S.12: Lagrangian tracer analysis: maps of the mean residence time and preferential pathways throughout Lake Llanquihue. Left panels show results from the autumn-winter (AW) season (Jun-1-2016/Aug-1-2016), whereas right panels show results from the spring-summer (SS) season (Dec-1-2016/Ma-1r-2017). The color bar denotes the time taken by lagrangian tracers released from Frutillar to reach the nearshore region of (a,e) Puerto Octay town, (b,f) Ensenada town, (c,g) Puerto Varas city, and (d,h) Llanquihue town.

Figure S.12 characterizes the time taken by particles to travel from Frutillar to Puerto Octay (panels a and e), Ensenada (panels b and f), Puerto Varas (panels c and g), and Llanquihue (panels d and h). In the AW season, particles reaching Puerto Octay and Ensenadas follow a pathway initially parallel to the shore, with the coastline at their left, until they connect to the LSC cyclonic gyre that transports them through pelagic waters to their target destinations (Figure S.12a,b). In the SS season, although particles also stream cyclonically, their pathway is much more confined to the shoreline (Figure S.12e,f). In contrast, to get into the littoral zones of Llanquihue and Puerto Varas, particles prefer following an anti-cyclonic pathway, keeping the coastline to their right (Figure S.12c,d).

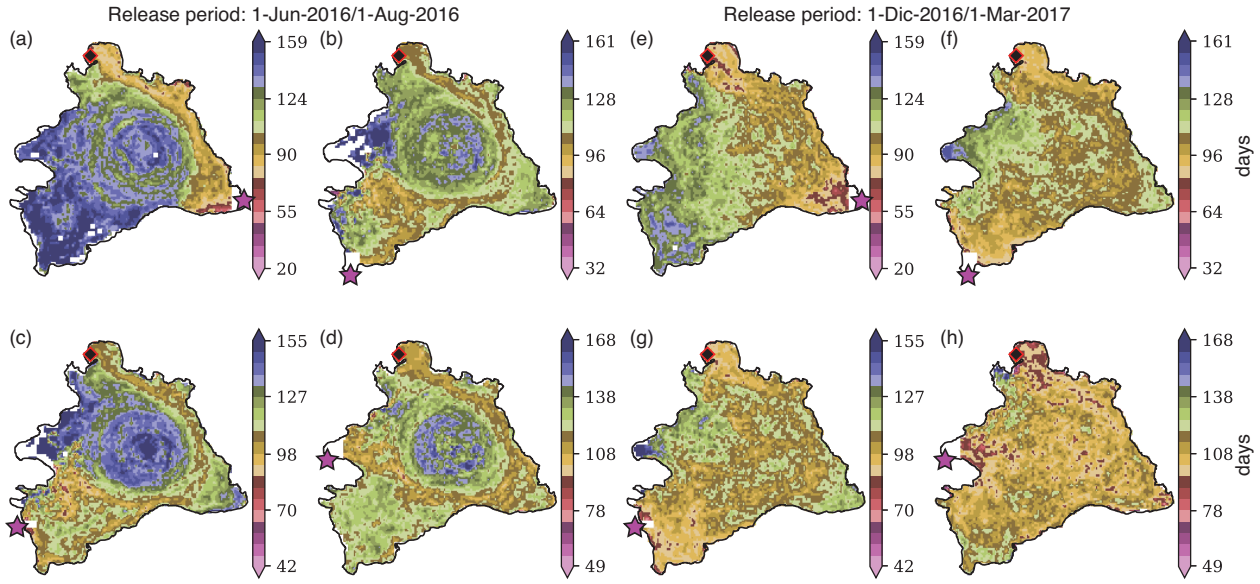

Figure S.13: Lagrangian tracer analysis: maps of the mean residence time and preferential pathways throughout Lake Llanquihue. Left panels show results from the autumn-winter (AW) season (Jun-1-2016/Aug-1-2016), whereas right panels show results from the spring-summer (SS) season (Dec-1-2016/Mar-1-2017). The colorbar in day units denotes the time taken by lagrangian tracers released from Puerto Octay to reach the nearshore region of (a,e) Ensenada town, (b,f) Puerto Varas city, (c,g) Llanquihue city, and (d,h) Frutillar city.

Similarly, Figure S.13 characterizes the time taken by particles to travel from Puerto Octay to Ensenada (panels a and e), Puerto Varas (panels b and f), Llanquihue (panels c and g), and Frutillar (panels d and h). From this site, particles follow a cyclonic pathway to reach the different littoral areas, taking advantage of the LSC gyre circulation.